Cell Metabolism

Article

Obesity-associated hyperleptinemia alters the gliovascular interface of the hypothalamus to promote hypertension

Graphical abstract

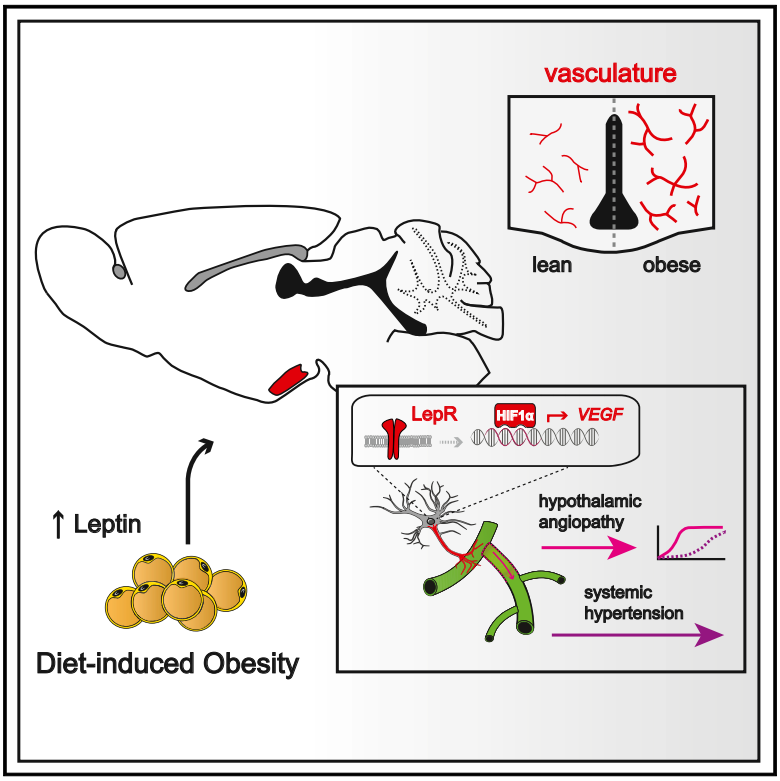

Authors

Tim Gruber, Chenchen Pan, Raian E. Contreras, ..., Tamas L. Horvath, Matthias H. Tschöp, Cristina García-Cáceres

Correspondence

matthias.tschoep@helmholtz-muenchen.de (M.H.T.), garcia-caceres@helmholtz-muenchen.de (C.G.-C.)

In brief

Here, Gruber et al. show that during diet-induced obesity in mice there is a profound remodeling of the gliovascular interface in the hypothalamus, resulting in arterial hypertension. This process is driven by elevated leptin levels and upregulation of a HIF1α-VEGF signaling axis in local astrocytes.

Highlights

- The hypothalamic gliovascular interface is dynamically remodeled during obesity
- Circulating leptin couples hypercaloric states with hypothalamic microangiopathy
- Leptin-induced astroglial HIF1α-VEGF drives angiogenesis in the hypothalamus
- VEGF in astrocytes promotes the development of arterial hypertension during obesity

Gruber et al., 2021, Cell Metabolism *33*, 1155–1170
June 1, 2021
https://doi.org/10.1016/j.cmet.2021.04.007

CellPress

Cell Metabolism

CellPress
OPEN ACCESS

Article

Obesity-associated hyperleptinemia alters the gliovascular interface of the hypothalamus to promote hypertension

Tim Gruber,[1,2,3] Chenchen Pan,[4,5] Raian E. Contreras,[1,2,6,7] Tobias Wiedemann,[8] Donald A. Morgan,[9] Alicja A. Skowronski,[10] Sandrine Lefort,[1,2] Cahuê De Bernardis Murat,[1,2] Ophelia Le Thuc,[1,2] Beata Legutko,[1,2] Francisco J. Ruiz-Ojeda,[2,11] María de la Fuente-Fernández,[12] Angel Luis García-Villalón,[12] Daniel González-Hedström,[12] Melanie Huber,[1,2] Klara Szigeti-Buck,[13] Timo D. Müller,[1,2,14] Siegfried Ussar,[2,11,15] Paul Pfluger,[1,2,6,7] Steve C. Woods,[16] Ali Ertürk,[4,5] Charles A. LeDuc,[10] Kamal Rahmouni,[9] Miriam Granado,[12] Tamas L. Horvath,[3,13] Matthias H. Tschöp,[1,2,17,*] and Cristina García-Cáceres[1,2,18,19,*]

[1]Institute for Diabetes and Obesity, Helmholtz Diabetes Center, Helmholtz Zentrum München, German Research Center for Environmental Health (GmbH), 85764 Neuherberg, Germany
[2]German Center for Diabetes Research (DZD), 85764 Neuherberg, Germany
[3]Institute for Advanced Studies, Technische Universität, 85748 Garching, Germany
[4]Institute for Tissue Engineering and Regenerative Medicine (ITERM), Helmholtz Zentrum München, German Research Center for Environmental Health (GmbH), 85764 Neuherberg, Germany
[5]Institute for Stroke and Dementia Research, Klinikum der Universität München, Ludwig Maximilian University of Munich (LMU), 81377 Munich, Germany
[6]Research Unit Neurobiology of Diabetes, Helmholtz Zentrum München, 85764 Neuherberg, Germany
[7]Neurobiology of Diabetes, TUM School of Medicine, Technical University Munich, 80333 Munich, Germany
[8]Institute for Diabetes and Cancer, Helmholtz Diabetes Center, Helmholtz Zentrum München, German Research Center for Environmental Health (GmbH), 85764 Neuherberg, Germany
[9]Department of Neuroscience and Pharmacology, University of Iowa, Iowa City, IA, USA
[10]Division of Molecular Genetics, Department of Pediatrics, Vagelos College of Physicians and Surgeons, Naomi Berrie Diabetes Center, Columbia University Irving Medical Center, New York, NY, USA
[11]RG Adipocytes & Metabolism, Institute for Diabetes & Obesity, Helmholtz Diabetes Center, Helmholtz Zentrum München, German Research Center for Environmental Health GmbH, 85764 Neuherberg, Germany
[12]Physiology Department, School of Medicine, Universidad Autónoma de Madrid, Madrid, Spain
[13]Program in Integrative Cell Signaling and Neurobiology of Metabolism, Section of Comparative Medicine, Yale University School of Medicine, New Haven, CT, USA
[14]Department of Pharmacology and Experimental Therapy, Institute of Experimental and Clinical Pharmacology and Toxicology, Eberhard Karls University Hospitals and Clinics, Tübingen, Germany
[15]Department of Medicine, Technische Universität, Munich, Germany
[16]Department of Psychiatry and Behavioral Neuroscience, University of Cincinnati, Cincinnati, OH, USA
[17]Division of Metabolic Diseases, Department of Medicine, Technische Universität, Munich, Germany
[18]Medizinische Klinik and Poliklinik IV, Klinikum der Universität, Ludwig-Maximilians-Universität München, Munich, Germany
[19]Lead contact
*Correspondence: matthias.tschoep@helmholtz-muenchen.de (M.H.T.), garcia-caceres@helmholtz-muenchen.de (C.G.-C.)
https://doi.org/10.1016/j.cmet.2021.04.007

SUMMARY

Pathologies of the micro- and macrovascular systems are a hallmark of the metabolic syndrome, which can lead to chronically elevated blood pressure. However, the underlying pathomechanisms involved still need to be clarified. Here, we report that an obesity-associated increase in serum leptin triggers the select expansion of the micro-angioarchitecture in pre-autonomic brain centers that regulate hemodynamic homeostasis. By using a series of cell- and region-specific loss- and gain-of-function models, we show that this pathophysiological process depends on hypothalamic astroglial hypoxia-inducible factor 1α-vascular endothelial growth factor (HIF1α-VEGF) signaling downstream of leptin signaling. Importantly, several distinct models of HIF1α-VEGF pathway disruption in astrocytes are protected not only from obesity-induced hypothalamic angiopathy but also from sympathetic hyperactivity or arterial hypertension. These results suggest that hyperleptinemia promotes obesity-induced hypertension via a HIF1α-VEGF signaling cascade in hypothalamic astrocytes while establishing a novel mechanistic link that connects hypothalamic micro-angioarchitecture with control over systemic blood pressure.

INTRODUCTION

Both macro- and microvascular complications are comorbidities of obesity, and vascular dysfunction is considered to be a primary factor in the increased risk of obesity-associated mortality and disability (Flegal et al., 2013; Poirier et al., 2006). While obesity often leads to damage of macrovessels in the form of atherosclerosis and arterial hypertension, the microvascular compartment is also frequently pathologically restructured. Importantly, macrovascular hypertension is widely regarded both to precede and to functionally contribute to the development of microvascular remodeling by inducing increased capillary pressure (Folkow et al., 1958). As extensively documented with regard to the retina, kidney, and peripheral nerves, microvascular instability and neovascularization confer the major threat of progressive organ failure and risk of disability during diabetes and obesity (Rask-Madsen and King, 2013).

Microvascular remodeling, however, is not solely restricted to peripheral tissues and can occur within the brain. For example, consumption of a high-calorie diet induces a peculiar remodeling of the hypothalamic microvasculature that is observable in both mice and humans (Yi et al., 2012). Intrigued by this observation, we interrogated whether hypothalamic hypervascularization during diet-induced obesity (DIO) is a prerequisite for the development of arterial hypertension. We also explored the involvement of astrocytes, as these cells are an integral cell type of the neurovascular unit, which forms direct physical contacts with cerebral blood vessels via their perivascular endfeet (Mathiisen et al., 2010). Because astrocytes occupy such a privileged position within the brain parenchyma, we hypothesized that they are ideally situated to survey the metabolic status of the organism and, in turn, to homeostatically and pathologically remodel local vascular beds.

Astrocytes critically contribute to the formation and maintenance of the blood-brain barrier (BBB) via both physical contact and by releasing an array of soluble factors. The gliovascular interface has thus attracted considerable interest toward brain-based pharmacotherapies, and much effort is being placed on the understanding of how astrocytes modulate BBB function and, more specifically, whether astrocytes might control the selective access of some circulating factors into the brain. Consistent with this role, our previous studies have demonstrated that astrocytes regulate the accessibility of circulating factors (lipids, glucose, and hormones) within the brain and in turn cooperate with neurons in the regulation of feeding and systemic glucose metabolism (Kim et al., 2014; Gao et al., 2017; García-Cáceres et al., 2016, 2019).

It remains to be elucidated if and how this structural remodeling at the gliovascular interface contributes to the initiation and progression of obesity. Here, we report that feeding a high-fat, high-sugar (HFHS) diet to mice induces rapid-onset microvascular remodeling within the hypothalamus, including within pre-autonomic centers, and that this occurs prior to changes in systemic arterial blood pressure but concurrent with substantial diet-induced body weight gain and elevated serum leptin levels. Moreover, both local astrocytes and the vasculature in the hypothalamus undergo profound pathological changes that are not found elsewhere in the brain. We further found that the hypoxia-inducible factor 1α-vascular endothelial growth factor (HIF1α-VEGF) pathway acts downstream of leptin signaling in hypothalamic astrocytes, and that HFHS diet feeding and hyperleptinemia trigger the pathological reorganization of the local angioarchitecture. Collectively, these findings reveal the unprecedented involvement of astrocytes in the mediobasal hypothalamic regulation of systemic blood pressure. Furthermore, these findings identify a hitherto unrecognized functional link between astrocyte-mediated dynamic remodeling of the hypothalamic vasculature and the regulation of systemic blood pressure in response to high-calorie diets and elevated leptin levels.

RESULTS

HFHS diet feeding induces microangiopathy specifically in the hypothalamus and prior to the development of systemic hypertension in mice.

Feeding an obesogenic diet to mice induces vascular dysfunction in various organ systems over time, and it is frequently used to model human obesity-related cardiovascular complications. Here, we compared the temporal development of diet-induced damage of blood vessels in the periphery versus in the brain of C57BL/6J mice. Consistent with previous observations (Ternacle et al., 2017; Oishi et al., 2018), the systemic elevation of arterial blood pressure was manifested upon chronic, but not short-term, exposure to a HFHS diet in comparison to a standard chow (SC) diet (Figure 1A). In contrast, neovascularization of the hypothalamus, which was recently identified as a consequence of high-calorie exposure (Yi et al., 2012), occurred more rapidly, becoming significant after only 2 weeks of HFHS diet feeding (Figure 1A). By combining fluorescent angiography, optical tissue clearing, and 3D imaging of the entire mouse brain vasculature (Ertürk et al., 2012), we observed that diet-induced cerebrovascular remodeling was restricted to specific hypothalamic nuclei where the local microenvironment seemed to be susceptible to hypervascularization upon HFHS exposure (Figures 1B and 1C; Video S1). Notably, we additionally observed that a substantial proportion of these more abundant vessels display signs of HFHS diet-induced structural and functional impairments, as previously reported in other tissues from individuals with obesity, diabetes mellitus, or hypertension (Roggendorf et al., 1988; Tsilibary, 2003). Specifically, we found that hypothalamic capillaries of HFHS diet-fed mice exhibit a discontinuous coverage by Claudin-5, an essential component of tight-junctions at the BBB (HFHS diet: −15.17% ± 1.48% Claudin-5 vessel coverage versus SC diet: −3.97% ± 0.65% Claudin-5 vessel coverage; data not shown). Furthermore, these structural changes were associated with higher extravasation of serum proteins, such as albumin (vascular hyperpermeability), suggesting functional impairment in barrier properties (Figures 1D and S1A; HFHS diet: 1.94% ± 0.57% extravascular pixels versus SC diet: 0.48% ± 0.06% extravascular pixels; data not shown). In addition, these hypothalamic microvessels had a marked thickening in their basement membrane as evidenced by greater deposition of extracellular matrix proteins, collagen-IV (HFHS diet: 2.64 ± 0.13 μm versus SC diet: 1.76 ± 0.19 μm), and laminin (HFHS diet: 2.67 ± 0.2 μm versus SC diet: 1.61 ± 0.2 μm; Figure 1E). Using electron microscopy, we further confirmed ultrastructural alterations in the hypothalamic microvasculature of DIO mice and found that chronic HFHS diet exposure resulted in significant thickening of the

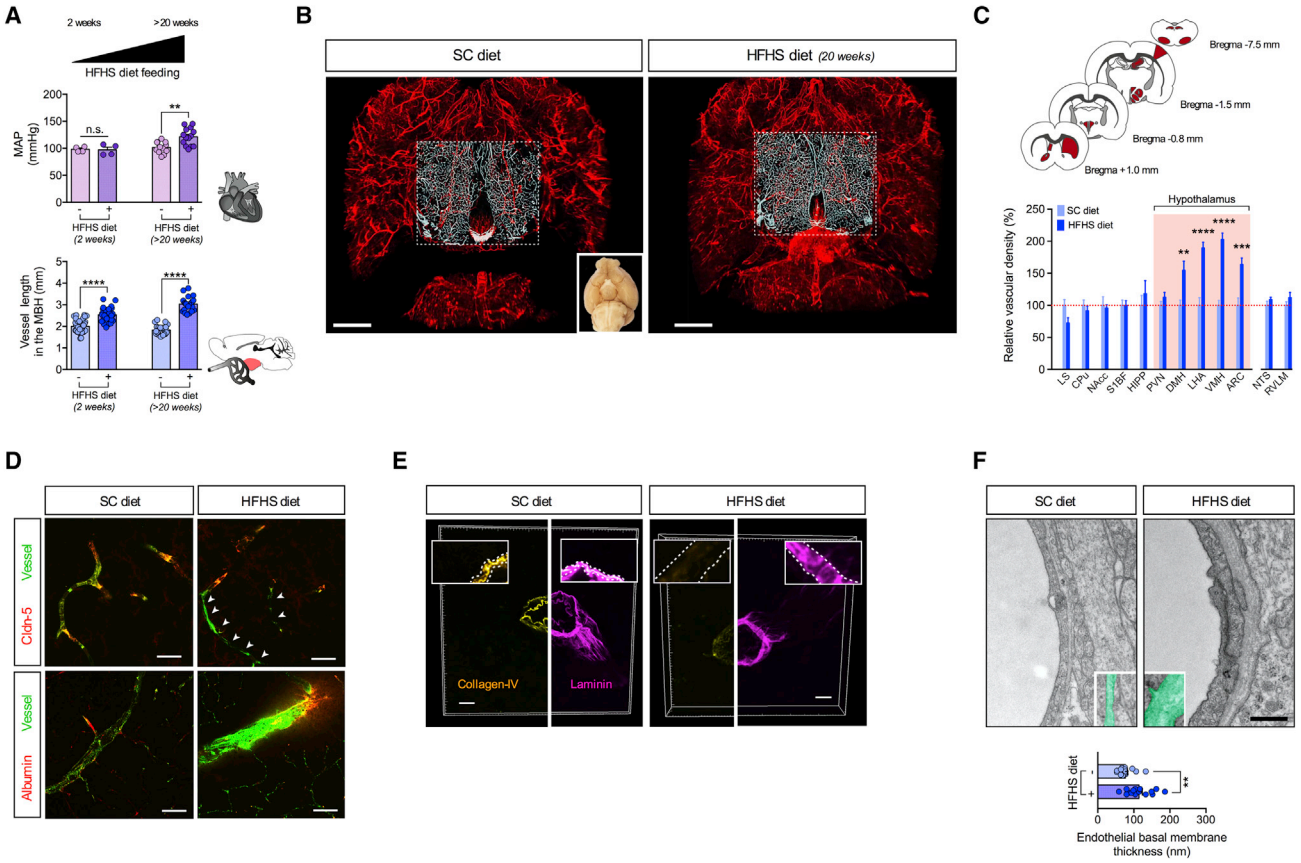

Figure 1. HFHS diet feeding induces hypervascular microangiopathy specifically in the hypothalamus

(A) Mean arterial blood pressure (MAP) and vessel length in the mediobasal hypothalamus (MBH) of C57BL/6J mice fed a high-fat, high-sugar (HFHS) diet for 2 or >20 weeks in comparison to a standard chow (SC) diet. Data are represented as a mean MAP of individual mice repeatedly measured over separate days and as total vessel length per individual MBH hemisection. n = 4–7 mice per group (blood pressure) and n = 6–7 mice (fluorescent angiography); 6–8 hemisections/mouse.

(B) Light-sheet microscopy images (ventral views) of the 3D whole-brain angioarchitecture in mice fed SC or HFHS diet. Images are representative of data in (C).

(C) Quantitative assessment of HFHS diet-induced vascular density in different brain regions relative to an SC diet. LS, lateral septum; CPu, caudate-putamen; NAcc, nucleus accumbens; S1BF, somatosensory cortex, barrel field; HIPP, hippocampus; PVN, paraventricular nucleus; DMH, dorsomedial hypothalamus; LHA, lateral hypothalamus; VMH, ventromedial hypothalamus; ARC, arcuate nucleus; NTS, nucleus tractus solitarius; RVLM, rostral ventrolateral medulla. n = 3 mice per group; consecutive focal planes (z-step: 8 μm) were cropped out according to the brain region and individually analyzed; each brain region was analyzed from both hemispheres.

(D) Confocal micrographs of hypothalamic microvessels (green), Claudin-5 (red; upper panel), and albumin (red; lower panel) in mice fed with an SC or HFHS diet.

(E) High-resolution 3D-rendered confocal micrographs of cross-sectional hypothalamic microvessels (∅ = 4–8 μm) depicting collagen-IV (yellow) and laminin (magenta) in mice fed with an SC or HFHS diet.

(F) Representative electron micrographs of hypothalamic microvessels of mice fed with an SC or HFHS diet, with highlighted endothelial basal membranes. Below, the quantification of the endothelial basal membrane thickness. n = 3–6 mice per group; 4–6 ultra-thin sections/mouse.

Scale bars, 200 μm (B), 10 μm (D and E), and 500 nm (F). **p < 0.01, ***p < 0.001, and ****p < 0.0001. n.s., not significant. Statistical tests included unpaired Student's t test (A, C, and F).

endothelial basal membrane than SC-diet-fed mice (Figure 1F). Overall, these results reveal a particular vulnerability of distinct hypothalamic nuclei to develop hypervascular microangiopathy in response to short-term HFHS diet feeding, and it precedes any changes in systemic blood pressure.

Hypothalamic microangiopathy occurs at the onset of bodyweight gain and coincides with increased circulating leptin

Obesogenic diets have previously been described to trigger profound cellular rearrangements affecting the cytoarchitecture of the hypothalamus (Horvath et al., 2010), several of which occur with remarkable rapidity and prior to any metabolic disturbances in the periphery (Thaler et al., 2012). We therefore sought to temporally pinpoint the exact initiation of the hypothalamic angiogenic response to HFHS diet feeding to determine if it occurs prior to or secondary to bodyweight gain. As previously reported by others (Williams et al., 2014), a 5-day HFHS diet feeding was sufficient to impair peripheral glucose tolerance in normal-weight mice relative to an SC diet (Figure S1B) but with no apparent changes in hypothalamic vessel density (Figure S1B). Likewise, a prolonged period of severe hyperglycemia

in a non-obese mouse model of streptozotocin (STZ)-induced type 1 diabetes led to only a slight tendency of hypothalamic neovascularization (Figure S1C), which was of far smaller magnitude overall when compared with changes upon chronic HFHS diet feeding (Figure 1C). Together, these findings argue against a major causal role of impaired glucose metabolism in the process of hypothalamic vessel remodeling.

In contrast, the onset of hypothalamic hypervascularization in HFHS diet-fed mice occurred at the time when bodyweight started to significantly diverge between mice fed with an HFHS diet or SC diet, i.e., after 15 days of diet exposure (Figures 1A and 2A). Notably, this process was accompanied by higher expression of pro-angiogenic signaling cues in the hypothalamus, but not in the cortex (Figure S2D), with VEGF being among the most robustly induced factors among those elevated in response to HFHS diet feeding (Figures 2B and S2A). Notably, the moment of hypothalamic hypervascularization was not only concurrent with the moment of significant body weight gain but also coincided with the onset of higher leptin levels with HFHS diet feeding (Figure 2C). We thus conclude that, whereas hypothalamic vascularization is not modulated by elevated blood glucose levels, it is associated with a significantly higher expression of pro-angiogenic genes in the hypothalamus, as well as increased body weight and elevated circulating leptin levels with an HFHS diet.

Hypothalamic hypervascularity in mice is reversed by diet-induced weight loss and normalization of serum leptin levels

We next sought to investigate if hypothalamic hypervascularization in mice could be reversed by a diet-based weight loss intervention. We thus switched DIO mice back to an SC diet for 5 weeks to reduce excess bodyweight and fat mass (Figure S2B), along with serum leptin levels (Figure S2C). As revealed by post hoc fluorescent angiography, diet reversal potently normalized the hypothalamic vessel profile to levels seen in lean control mice solely fed with an SC diet (Figure 2D). In order to determine if microvascular remodeling in the hypothalamus was specifically dependent on an altered diet composition or more generally the result of reduced caloric intake and body fat loss, we included a calorie-restricted (CR) group given 70% of their *ad libitum* HFHS diet intake (Figure 2E). Notably, a strong positive linear relationship ($r^2 = 0.8046$) was found between the extent of hypothalamic vascularity and the degree of adiposity across all four groups (Figure 2E). Moreover, hypothalamic vascular profiles in lean, DIO, CR, and diet-reversed—i.e., formerly DIO—mice mirrored the number of $VEGF^+$ cells in the MBH and serum leptin levels (Figures 2F and 2G, respectively). Overall, these results suggest that the derangement of microvascular networks in the hypothalamus in response to DIO constitutes a dynamic process that can be reversed upon weight loss. Furthermore, we found that changes in circulating leptin levels are associated with the extent of hypothalamic vascularity.

Leptin signaling in the brain rather than obesity per se acts as a driver in the development of hypothalamic neovascularization

Given the substantial cross-correlation between adiposity and leptin levels, we aimed to functionally disentangle whether hypothalamic microangiopathy is driven by HFHS diet-induced signals such as leptin, as opposed to adiposity per se. Thus, we profiled monogenetically obese leptin-deficient ($Lep^{ob/ob}$) and leptin receptor-deficient ($Lep^{db/db}$) mice maintained on an SC diet. Despite the substantial adiposity of these models relative to their respective heterozygous littermate controls (Figure S3A), the hypothalamic vessel density remained entirely unchanged in $Lep^{ob/ob}$ and $Lep^{db/db}$ mice (Figure 3A), both of which are characterized by the single commonality of absent leptin signaling. Intrigued by the different vascular profiles of these two genetically obese mouse models as compared with DIO mice and, given that leptin receptor (LepR) is highly expressed in the MBH (Figure S3B), we further explored a putative involvement of leptin in promoting hypothalamic neovascularization. Thus, we tested this hypothesis by treating leptin-deficient $Lep^{ob/ob}$ mice with an HFHS diet or exogenous leptin. While 14 days of HFHS diet feeding in $Lep^{ob/ob}$ mice did not lead to a greater hypothalamic vessel density, central leptin infusion resulted in significant and robust hypervascularization of the MBH at both a low dose (50 ng/day for 10 days) as well as a higher dose (200 ng/day for 7 days) (Figure 3A). Importantly, this expansion in microvascular density occurred under the state of rapid and pronounced bodyweight loss (−25.8% ± 0.87% at termination), supporting that leptin signaling, rather than other aspects of obesity, confers pro-angiogenic stimulation in the hypothalamus. To further disentangle the confounding cross-correlation between serum leptin and body fat ($r^2 = 0.9260$; Figure S3C), we employed a transgenic mouse model (TRE-Lep^{rtTA}) to induce overexpression of leptin by adding doxycycline (DOX) to the drinking water (Skowronski et al., 2020). Exposing these lean mice to DOX for 4 weeks rendered them significantly hyperleptinemic (Figure S3C). Yet, such hyperleptinemia was sufficient to promote a significantly higher vascular density of the MBH when compared with littermate controls (TRE-Lep) also receiving DOX but without leptin elevation (Figure 3A). Consistently, DOX-induced leptin overexpression and repeated pharmacological leptin administration to lean C57BL/6J mice (3 mg/kg BW i.p. twice daily for 3 days; Figure 3B) led to significantly higher levels of endothelial proliferation markers such as *Ki67*, *Vegfr2/Kdr*, and *Cd105/endoglin* (Figures 3C and S3D), as well as pro-angiogenic VEGF expression within the hypothalamus (Figure 3D). Interestingly, the rise of hypothalamic VEGF expression in exogenous leptin-infused mice exceeded the effect of 2-week feeding with an HFHS diet (Figure 3D). Conversely, VEGF expression levels were unaltered in the MBH of both $Lep^{db/db}$ mice and $Lep^{ob/ob}$ mice, despite massive obesity (Figure 3D).

Next, we aimed to disentangle whether the normalization of vascularity and VEGF expression upon weight loss (Figures 2D–2F) are driven by hyperleptinemia rather than adiposity per se. To address this question, we pharmacologically maintained elevated leptin levels in formerly DIO mice undergoing diet reversal (1 mg/kg BW every other day, s.c.) and observed that elevated leptin levels abrogated the normalization of hypothalamic vascular profiles (Figure 3E). Prompted by these findings in the hypothalamus, we next sought to investigate if the interrelations among adiposity, serum leptin, and neurovasculopathy would extend to other tissues, such as those of the eye, which contain neurovascular beds that are highly susceptible to metabolic damage. However, while HFHS diet feeding over the

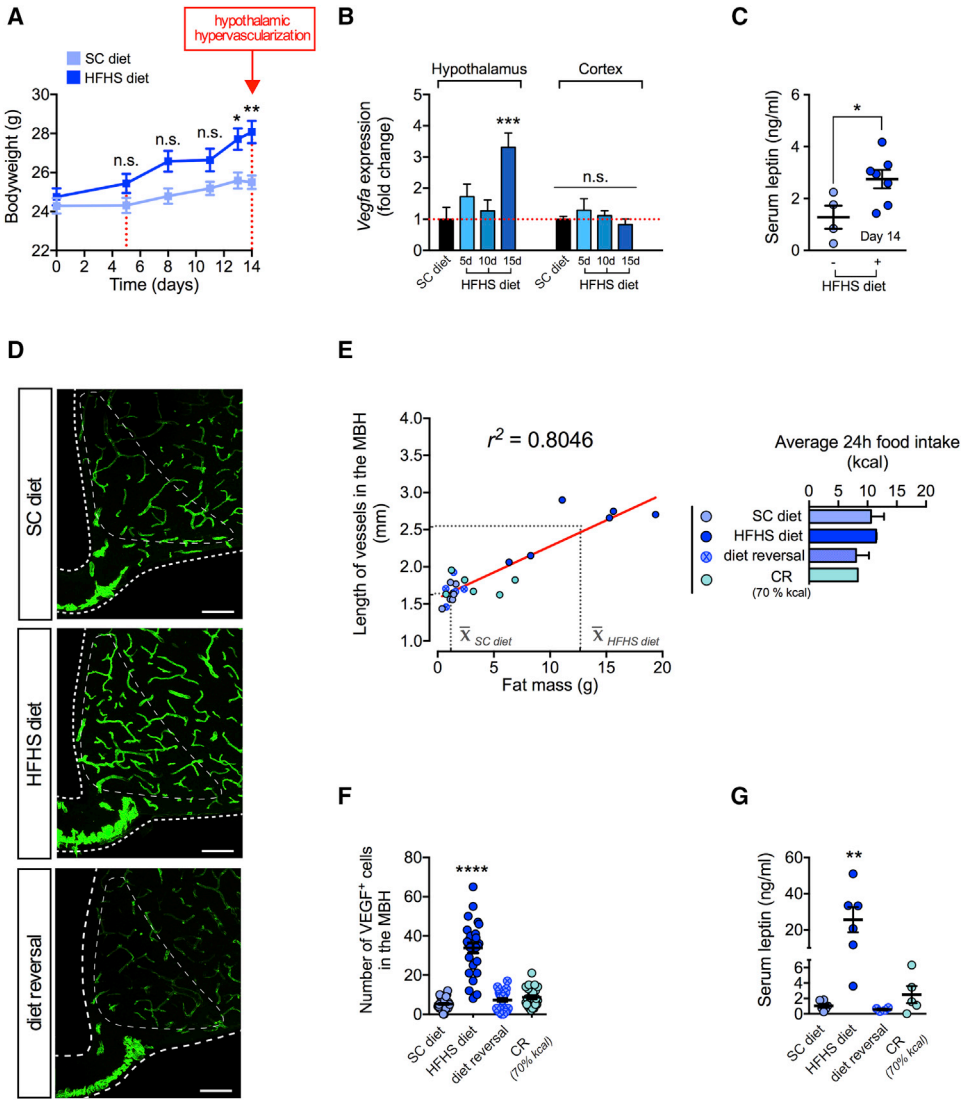

Figure 2. Hypothalamic vascularity is rapidly and dynamically altered by HFHS diet feeding in association with circulating leptin levels

(A) Bodyweight of SC and HFHS diet-fed mice. The red arrow indicates the onset of HFHS-induced hypothalamic hypervascularization in mice (see Figure 1A). n = 4–7 mice per group.

(B) mRNA expression of vascular endothelial growth factor A (*Vegfa*) in the hypothalamus and cortex from mice fed with an SC diet and an HFHS diet at different time points. n = 8 mice per group.

(C) Serum leptin levels in mice fed with an SC diet or 14-day HFHS diet. Data are presented as individual mice and mean ± SEM. n = 4–7 mice per group (unpaired t test).

(D) Confocal micrographs depicting the MBH vessel profile of SC diet-fed, HFHS diet-fed, and diet-reversed (DR) mice. Data are representative of the cohort depicted in Figure S1G.

(E) Linear regression analysis between the length of vessels in the MBH and the body fat mass of mice fed SC, HFHS, DR, and calorie-restricted (CR) diet. The average 24-h food intake of respective groups is shown on the right. n = 6 mice per group.

(F) Quantification of the number of VEGF$^+$ cells in the MBH between groups. Data are represented as individual hemisection and mean ± SEM. n = 6 mice per group; 6–8 hemisections/mouse.

(G) Quantification of serum leptin levels between groups. n = 6 mice per group.

Scale bars, 100 μm (D). *p < 0.05, **p < 0.01, ***p < 0.001, and ****p < 0.0001. n.s., not significant. Statistical tests included two-way ANOVA (A), one-way ANOVA (B, F, and G), and unpaired Student's t test (C).

course of 4 months induced marked hypothalamic hypervascularity, it failed to change vascular density in the retina, as assessed in whole retinal flat mounts in mice (data not shown), suggesting separate tissue-specific mechanisms underlying microvascular remodeling in DIO mice.

Next, we assessed the protein levels of the hypoxia-inducible factor 1 alpha (HIF1α), the direct transcriptional regulator of VEGF in the hypothalamus and found that hypothalamic HIF1α levels tended to be higher in response to HFHS diet feeding and an acute leptin administration (5 mg/kg BW i.p.). Notably,

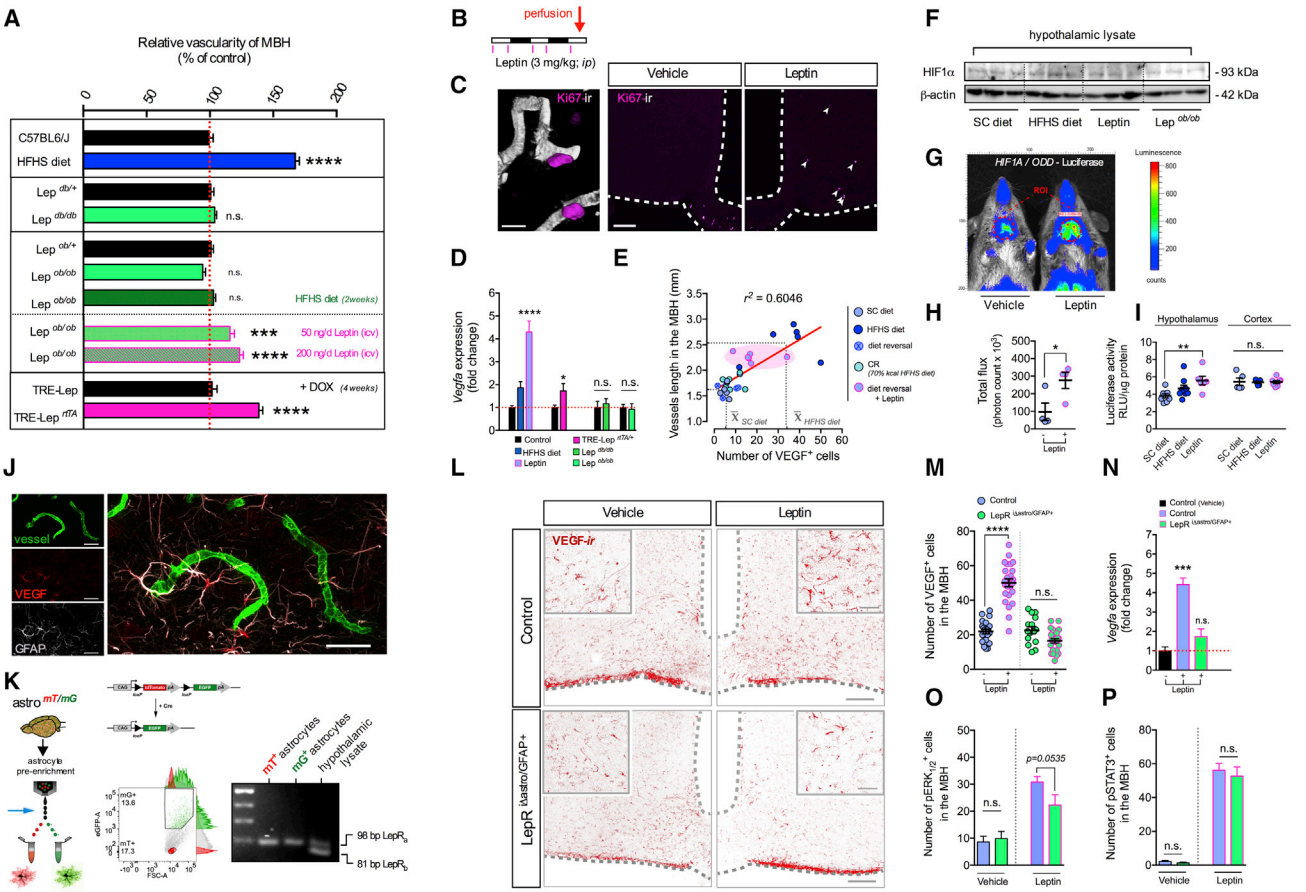

Figure 3. Leptin signaling induces pro-angiogenic signaling in the hypothalamus

(A) Quantification of MBH vascularity in diet-induced obese C57BL/6J mice, genetically obese SC diet-fed Lep $^{db/db}$ mice, Lep $^{ob/ob}$ mice fed SC diet or HSHS diet (2 weeks) or receiving one of two doses of chronic leptin minipump infusions into the lateral ventricle (50 or 200 ng/day, respectively), and leptin-overproducing TRE-Lep ^{rtTA} mice receiving doxycycline in the drinking water (4 weeks). Data are presented relative to respective controls as indicated. n = 4–6 mice per group; 6–8 hemisections/mouse.

(B) Experimental paradigm of repeated leptin injections (3 mg/kg i.p.) twice daily for 2 days in the morning and the evening with a terminal injection prior to sacrifice.

(C) High-power confocal micrographs of hypothalamic vasculature (white) exhibiting cells immunoreactive for Ki67^{+} (magenta) from mice treated with leptin or vehicle.

(D) Whole hypothalamic gene expression of *Vegfa* mRNA of C57BL/6J mice fed 15-day HFHS diet or receiving repeated leptin injections according to (B); TRE-Lep ^{rtTA} mice receiving doxycycline in the drinking water (4 weeks) and *Vegfa* expression of MBH micropunches from Lep $^{db/db}$ mice and Lep $^{ob/ob}$ mice. Data are presented relative to respective controls. n = 7–14 mice per group.

(E) Linear regression analysis of the vessel length in the MBH and the number of VEGF^{+} cells of C57BL/6J mice fed SC diet or HFHS diet, or undergoing calorie restriction, diet reversal, or diet reversal with leptin re-substitution (1 mg/kg s.c. every other day). Arithmetic means of SC diet and HFHS diet indicated as dotted lines (gray). n = 6 mice per group.

(F) Western blot pictures depicting hypothalamic HIF1α protein content of C57BL/6J mice fed SC diet or HFHS diet, or acutely leptin-injected mice (5 mg/kg i.p.) and Lep $^{ob/ob}$ mice. n = 3 mice per group. Representative western blot of two independent experiments.

(G) Photographic-bioluminescent image of two anesthetized HIF1/ODD-luciferase mice that received either vehicle or exogenous leptin 60 min prior to bioluminescence *in vivo* imaging.

(H) Corresponding quantification of total photon flux from the ventral side of the head of HIF1/ODD-luciferase mice receiving either vehicle or exogenous leptin (5 mg/kg i.p.). n = 4 mice per group.

(I) Quantification of luciferase activity in hypothalamic or cortical lysates of HIF1/ODD-luciferase mice that were either fed with an SC diet or an HFHS diet (5 days), or acutely injected with leptin (5 mg/kg i.p.). n = 7 per group.

(J) Confocal micrographs depicting hypothalamic vessels (green), VEGF immunoreactivity (red), and GFAP-positive astrocytes (gray).

(K) Schematic illustration depicting the experimental design to detect the presence of LepR$_a$ and LepR$_b$ isoforms in hypothalamic astrocytes by employing astrocyte-specific, Cre-dependent dual fluorescent reporter mouse line, a representative FACS blot, and image of the gel electrophoretic separation of LepR$_a$ (98 bp) and LepR$_b$ (81 bp) amplicons upon RT-PCR.

(L) Confocal scans illustrating the VEGF immunoreactivity (red) in the MBH from mice lacking the LepR specifically in GFAP-positive astrocytes (LepR$^{i\Delta astro/GFAP+}$) and respective controls, both receiving repeated leptin injections or vehicle. Images are representative of data in (M).

(M) Corresponding quantification of VEGF immunoreactive cells within the MBH between groups. n = 3–4 mice per group; 6–8 hemisections/mouse.

(legend continued on next page)

obese leptin-deficient Lep$^{ob/ob}$ mice tended to have lower HIF1α protein levels in SC diet-fed, HFHS diet-fed, or leptin-injected mice (Figure 3F). We further confirmed the induction of HIF1α in response to leptin by using HIF1/ODD-luciferase mice, which exhibited significant increases in total photon flux during *in vivo* bioluminescence imaging from the ventral part of the head 60 min after leptin administration than vehicle injection (5 mg/kg BW; i.p.) (Figures 3G and 3H). Notably, leptin administration induced higher luciferase activity particularly in hypothalamic, but not cortical, protein lysates *ex vivo*, when compared with its administration in mice fed with an SC diet (Figure 3I). Overall, these findings indicate that leptin signaling, regardless of the adiposity grade, is a determining factor driving the upregulation of HIF1α-VEGF signaling as well as hypervascularization particularly in the hypothalamus of obese mice; a recurrent phenomenon observed in DIO mice but absent in Lep$^{ob/ob}$ and Lep$^{db/db}$ mice.

Astrocytes are the main cellular source of HFHS diet-induced VEGF in the hypothalamus

To identify the cellular source of hypothalamic VEGF production upon either HFHS diet feeding or leptin treatment, we conducted an array of double-immunohistochemical staining. VEGF immunoreactivity (ir) was revealed to exclusively co-localize with astrocytes positive for glial fibrillary acidic protein (GFAP$^+$) (Figure 3J), while being absent from both neurons (NeuN$^+$) and microglia (Iba1$^+$) (Figure S3E). Contrary to the traditionally held view, astrocytes constitute a diverse class of cells displaying substantial inter- and intraregional heterogeneity in their molecular profiles and function (Haim and Rowitch, 2017). Hence, we assessed hypothalamic astroglial VEGF-*ir* across two astroglial populations as identified by their expression of the astrocyte-enriched marker proteins GFAP and/or glutamate-aspartate transporter (GLAST). Over the course of this analysis, we noticed that VEGF-*ir* colocalized completely (100%) with astrocytes expressing GFAP filaments of perivascular endfeet independent of the presence of GLAST, suggesting a crucial role for GFAP in VEGF transport toward the endothelium (Table 1; Figure S3F). Thus, we repeated these co-immunostainings using brain sections of global GFAP$^{-/-}$ mice (Pekny et al., 1995) and observed a dramatic reduction in hypothalamic VEGF-*ir* that appeared disorganized and punctate (Figure S3G), further supporting the importance of GFAP-expressing astrocytes in gliovascular remodeling. To gain genetic access to this VEGF$^+$ subset of hypothalamic astrocytes, we first profiled the recombination pattern of human GFAP and GLAST-inducible Cre-driver lines (hGFAP.CreER^{T2} and GLAST.CreER^{T2}, respectively). To visualize postnatally tamoxifen-induced recombined astrocyte subpopulations, we crossed each of these astrocytic CreER^{T2}-driver lines with the Cre-dependent reporter mouse line ROSA26$^{mT/mG}$. The induction of VEGF immunoreactivity by HFHS diet feeding was found to be substantially attributable to both GFAP.CreER$^{T2/mG+}$ astrocytes (55.6%; N^0 = 188 cells; 3 mice) and GLAST.CreER $^{T2/mG+}$ astrocytes (65.9%; N^0 = 219 cells; 4 mice) (Figure S3H).

Leptin receptors in hypothalamic astrocytes regulate the production of VEGF in response to hyperleptinemia

To assess if the production of VEGF in hypothalamic astrocytes might be mediated by the direct influence of leptin, we sorted pre-enriched GLAST.CreER$^{T2/mG+}$ astrocytes by means of fluorescence-assisted cell sorting (FACS) to screen for the expression of both the short (LepR$_a$) and the long (LepR$_b$) leptin receptor isoforms by RT-PCR. In agreement with previous reports (Kim et al., 2014), we found that hypothalamic astrocytes express LepR (Figure 3K). Importantly, however, we only detected the truncated LepR$_a$, isoform in FACS-isolated GLAST-expressing astrocytes (mG$^+$), whereas no amplification of the long-form LepR$_b$ was found as compared with whole hypothalamic lysates (Figure 3K). Stimulation of the short LepR$_a$ isoform is known to robustly induce p42/44 MAPK (pERK$_{1/2}$) signaling, which we found was gradually more abundant in the MBH of mice upon either HFHS diet exposure (5 and 15 days) or repeated leptin injections (3 mg/kg BW i.p.; two times per day for 3 days) (Figure S3J). Among hypothalamic pERK$_{1/2}^+$ cells, we were able to detect a subset of astrocytes previously rendered identifiable by the cytosolic expression of a green fluorescent protein from the viral GFAP$_{(2.2\ kb)}$ promoter (Figure S3I). To assess if indeed the direct influence of leptin action in astrocytes leads to increased hypothalamic production of VEGF, we postnatally ablated LepR in hGFAP.CreER$^{T2/+}$ positive cells (LepR$^{i\Delta astro/GFAP+}$ mice), as previously described (Kim et al., 2014). Importantly, we observed that LepR$^{i\Delta astro/GFAP+}$ mice failed to exhibit higher VEGF levels in response to leptin administration, both on the protein as well as mRNA level, as compared with littermate control mice (Figures 3L–3N). Moreover, we observed a tendency for attenuated pERK$_{1/2}$ induction in the MBH of LepR$^{i\Delta astro/GFAP+}$ mice in response to repeated leptin administration (3 mg/kg BW i.p.; two times per day for 3 days) relative to wild-type littermate controls (Figure 3P). In contrast, no changes were detected in neuronal, LepR$_b$-dependent activation of pSTAT3 (Figure 3O). Additionally, we assessed hypothalamic vascularity in LepR$^{i\Delta astro/GFAP+}$ mice fed with an HFHS diet. Although leptin failed to increase hypothalamic VEGF-*ir* in these mice, LepR$^{i\Delta astro/GFAP+}$ mice still exhibited some degree of hypothalamic hypervascularization upon long-term HFHS diet feeding (Figure S3K). Importantly, however, the extent of HFHS diet-induced hypervascularity was significantly less pronounced in LepR$^{i\Delta astro/GFAP+}$ mice (125.2% ± 3.99% of SC diet control) as compared with wild-type littermates (147.1% ± 5.49% of SC

(N) Hypothalamic expression of *Vegfa* mRNA in control mice and LepR$^{i\Delta GFAP/+}$ mice both receiving exogenous leptin according to (B) or vehicle. n = 4–5 mice per group.

(O) Quantification of pERK$_{1/2}^+$ cells in the MBH of LepR$^{i\Delta GFAP/+}$ and control mice receiving leptin according to (B) or vehicle. n = 4–6 mice per group; 6–8 hemisections/mouse.

(P) Quantification of pSTAT3$^+$ cells in the MBH of LepR$^{i\Delta GFAP/+}$ and littermate control mice receiving leptin according to (B) or vehicle. n = 4–6 mice per group; 6–8 hemisections/mouse.

Scale bars, 10 μm (C [left panel] and L [inner panel]), 25 μm (J), and 100 μm (C [right panel] and L [outer panel]). ****$p < 0.0001$, ***$p < 0.001$, **$p < 0.01$, and *$p < 0.05$. n.s., not significant. Statistical tests included one-way ANOVA (A, D, I, and N) and unpaired Student's t test (A, H, M, O, and P).

Table 1. Colocalization of VEGF-*ir* with astrocytic population in the MBH

Diet	Number of VEGF$^+$ cells/hemisection MBH	% GFAP$^+$ astrocytes	% GLAST$^+$ (/GFAP$^+$) astrocytes
SC diet	6.416 ± 0.965 (n = 3)	100 ± 0	13.278 ± 3.979
5-day HFHS diet	12.166 ± 2.446 (n = 3)	100 ± 0	27.42 ± 5.892
15-day HFHS diet	13.1667 ± 0.588 (n = 3)	100 ± 0	42.428 ± 1.931

SC diet, standard chow diet; HFHS diet, high-fat/high-sugar diet; VEGF, vascular endothelial growth factor; GFAP, glial fibrillary acidic protein; GLAST, glutamate-aspartate transporter 1.

diet control). Collectively, these results suggest that astrocytes regulate the VEGF production in the hypothalamus upon $LepR_a$ activation while not being sufficient to fully prevent HFHS diet-induced hypothalamic hypervascularization.

Astrocyte-specific loss of HIF1α abrogates HFHS diet-induced VEGF expression and hypervascularization in the hypothalamus

The preponderance of evidence pointed us toward leptin as a stimulator of HIF1α-VEGF signaling in hypothalamic astrocytes during HFHS diet feeding. Thus, we generated genetic loss-of-function mouse models to assess whether the dynamic remodeling of the hypothalamic vasculature by HFHS diet feeding depends on the expression of HIF1α in either GFAP- and/or GLAST-expressing astrocytes. HIF1$\alpha^{loxP/loxP}$ mice were crossed with respective astrocytic CreER^{T2}-driver lines giving rise to knockout HIF1α in GFAP or GLAST-expressing astrocytes (HIF1$\alpha^{i\Delta astro/GFAP+}$ mice and HIF1$\alpha^{i\Delta astro/GLAST+}$ mice, respectively). Successful postnatal ablation of HIF1α was validated by backcrossing the Cre-dependent ROSA26$^{mT/mG}$ reporter line (Figure S4A) following two methods: (1) by comparing HIF1α expression after sorting non-recombined (tdTomato$^+$; red) and recombined (GFP$^+$; green) astrocytes collected from the same HIF1$\alpha^{i\Delta astro/GFAP+}$ mice (internal control: HIF1α downregulation in GFAP$^+$ astrocytes: 79.8% ± 0.09%; Figure S4B), and (2) by comparing HIF1α expression in recombined (GFP$^+$; green) astrocytes isolated from separate hGFAP.CreER^{T2}:ROSA26$^{mT/mG}$ reporter mice that harbor HIF1α alleles flanked by *loxP* sites as compared with mice carrying wild-type alleles (external control: HIF1α downregulation in GFAP$^+$ astrocytes: 43.5% ± 0.15%; Figure S4C).

Next, we challenged these mice with an HFHS diet and examined their capacity to increase astroglial VEGF production and vascular density in the MBH. Strikingly, HFHS diet-fed HIF1$\alpha^{i\Delta astro/GFAP+}$ mice were protected from excessive induction of VEGF expression in astrocytes compared with their corresponding HFHS diet-fed littermate controls (Figures 4A and 4B). In addition, the ablation of HIF1α from either GFAP$^+$ or GLAST$^+$ astrocytes abrogated the development of hypervascular angiopathy induced by HFHS diet feeding (Figure 4C). Besides the normalization of hypothalamic vessel density, astroglial HIF1α deletion averted several hypothalamic microvessel-glia abnormalities as observed in HFHS diet-fed mice (Figures 4D–4G). HFHS diet feeding in mice lacking HIF1α in astrocytes maintained endothelial coverage with the tight-junction protein claudin-5 (Figures 4D and S4E), showed an attenuated basement membrane thickening due to increased collagen-IV and laminin deposition (Figures 4E and S4D), and prevented the HFHS diet-induced increase in Iba$^+$ microglia in the MBH relative to littermate controls (Figures 4F and S4G), which was consistent with lower expression levels of pro-inflammatory *Tnf* (Figure S4F). Likewise, astroglial ablation of HIF1α abrogated vascular hyperpermeability to albumin and FITC-dextrans (40 kDa) as compared with HFHS diet-fed littermate controls (Figures 4G and 4H). Lastly, protection from HFHS diet-induced alterations at the glia-vascular interface was further corroborated at the ultrastructural level. Electron microscopic inspections revealed that HIF1$\alpha^{i\Delta astro/GFAP+}$ mice did not exhibit endothelial basal membrane thickening in response to HFHS diet when compared with HFHS diet-fed littermate controls (73.22 ± 5.82 nm versus 114.2 ± 9.22 nm, respectively).

Astrocyte-derived VEGF is sufficient for dynamic hypothalamic microvascular remodeling

In order to confirm that astrocyte-derived VEGF is the necessary and sufficient factor underlying the dynamic remodeling of the hypothalamic vasculature, we directly manipulated the expression of VEGF in astrocytes of the MBH by virus-mediated gene transfer (Figure S5A). First, we knocked down local VEGF expression in MBH astrocytes using small hairpin (sh)RNA expression (Figures S5B and S5C) driven from the long synthetic GFAP 2.2 kb promoter (Gfa2) and observed that the hypervascularization response to HFHS diet feeding was readily abrogated in the MBH of shRNA(VEGF)$^{GFAP+}$ mice (Figures 5A and 5B). We next restored VEGF expression in astrocytes otherwise devoid of HIF1α (Figure S5D). To accomplish this, we employed a dual virus approach and injected two separate vectors (AAV.Gfa2.iCre and AAV.Gfa2.VEGF$_{GFP}$, respectively) in order to (1) knockout HIF1α in MBH astrocytes and (2) concomitantly re-express VEGF in the injection site. Of all HIF1α-deficient astrocytes in the MBH (29.5 ± 4.63 per hemisection), roughly 30% were co-infected hence re-expressing transgenic VEGF (Figures S5E and S5F). Strikingly, we found that re-induction of astroglial VEGF expression in a fraction of HIF1$\alpha^{AAV.Gfa2.iCre}$ mice proved sufficient for promoting marked hypervascularization, even exceeding what is typically observed in HFHS diet-fed control mice (Figures 5D and 5E). Overall, these findings indicate that MBH astroglial VEGF is necessary and sufficient for developing hypothalamic angiopathy in response to HFHS diet feeding.

Blocking HIF1α or VEGF expression in MBH astrocytes prevents arterial hypertension and sympathetic hyperactivity in diet-induced obesity

Arterial hypertension is widely regarded as a significant contributor to microvascular remodeling and damage (Folkow et al., 1958; Feihl et al., 2008; de Montgolfier et al., 2019) However,

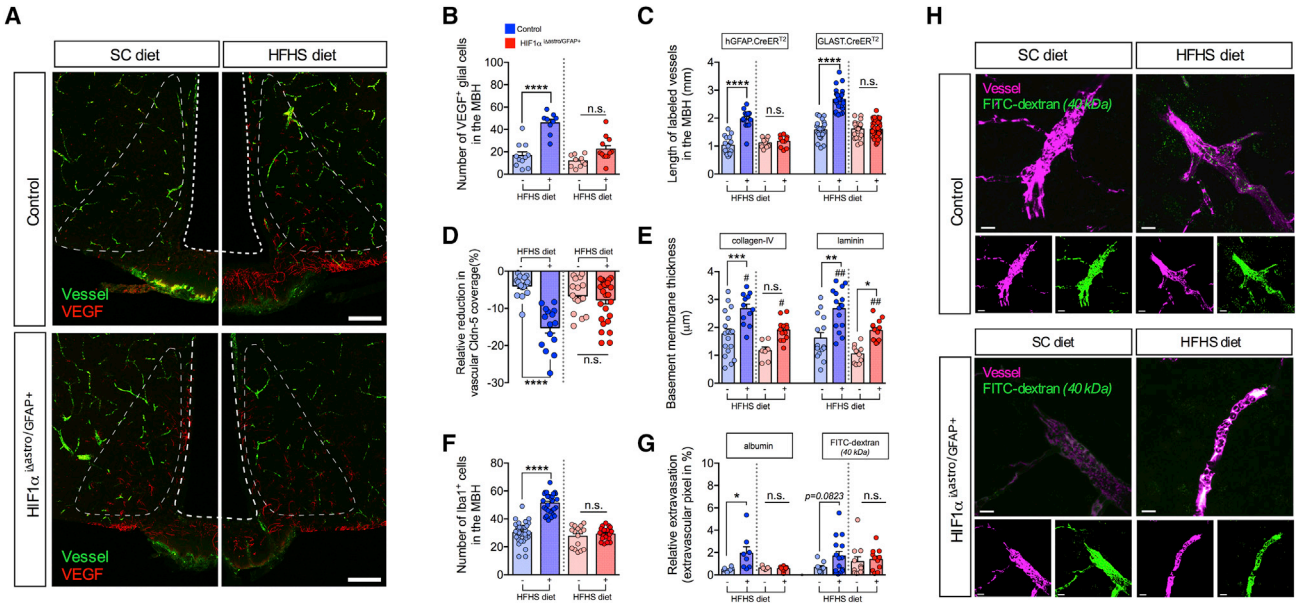

Figure 4. Astrocyte-specific loss of HIF1α abrogates VEGF upregulation and hypothalamic angiopathy in response to HFHS diet feeding

(A) Representative confocal micrographs depicting the vascular profile (green) and VEGF immunoreactivity (red) in the MBH of control mice and mice lacking HIF1α in GFAP-positive astrocytes (HIF1α$^{i\Delta astro/GFAP+}$) fed either with an SC or HFHS diet.

(B) Quantification of VEGF^{+} astrocytes in the MBH of control and HIF1α$^{i\Delta astro/GFAP+}$ mice fed with an SC or HFHS diet. n = 4–6 mice per group; 6–8 hemisections/mouse.

(C) Length of labeled vessels in the MBH from control mice and mice lacking HIF1α in hGFAP^{+} or GLAST^{+} cells either fed with an SC or HFHS diet. n = 4–6 mice per group; 6–8 hemisections/mouse.

(D) Quantification of microvascular claudin-5 coverage in control and HIF1α$^{i\Delta astro/GFAP+}$ mice fed either an SC or HFHS diet relative to entire vascular segment per field of view. n = 4–6 mice per group; 6–8 hemisections/mouse.

(E) Quantification of basement membrane thickness in control mice and mice lacking HIF1α in hGFAP^{+} or GLAST^{+} cells either fed with an SC or HFHS diet. n = 4–6 mice per group; 6–8 hemisections/mouse.

(F) Quantification of Iba1^{+} cells in the MBH of control and HIF1α$^{i\Delta astro/GFAP+}$ mice fed either an SC or HFHS diet. n = 4–6 mice per group; 6–8 hemisections/mouse.

(G) Quantification of relative extravasation of albumin and FITC-dextran (40 kDa) in control mice and mice lacking HIF1α in hGFAP+ or GLAST+ cells either fed with an SC or HFHS diet. n = 4–6 mice per group; 6–8 hemisections/mouse.

(H) High-power confocal micrographs of hypothalamic microvasculature of mice receiving i.v. injections of a vessel tracer (magenta; albumin-A647) along with an indicator of blood-brain barrier permeability (green; FITC-dextran).

Scale bars, 100 μm (A) and 10 μm (H). ****p < 0.0001, ***p < 0.001, **p < 0.01, and *p < 0.05. n.s., not significant. ##p < 0.01 and #p < 0.05 between HFHS diet groups of the respective genotypes. Statistical tests included unpaired Student's t test (B–G) and one-way ANOVA (E).

as our data indicate, HFHS diet-induced astroglial VEGF induction and hypervascularization of the hypothalamus occur significantly prior to diet-induced arterial hypertension (Figure 1A). This unexpected temporal succession prompted us to determine if microvascular abnormalities in hypothalamic pre-autonomic areas impact central hypertensive regulation upon HFHS diet feeding. Strikingly, mice receiving virus-mediated blockade of astroglial VEGF expression were protected from developing arterial hypertension upon an HFHS diet (Figure 5C), despite being as obese as control animals (Figure S5H). Of note, this depressor effect of mean arterial blood pressure (MAP) was entirely abolished in HIF1α $^{AAV.Gfa2.iCre}$ mice that additionally underwent a restoration of high VEGF expression by the same dual virus approach as described before (Figure 5F), despite no changes in bodyweight between groups (Figure S5I). Importantly, the marked protection from arterial hypertension in shRNA(VEGF)$^{GFAP/+}$ mice was independent of changes in serum leptin levels (Figure S5J) as well as basic endothelial function as measured by acetylcholine-induced vascular relaxation of aorta segments in obese shRNA(VEGF)$^{GFAP+}$ (Figure S5K). Instead, our data suggest that blockade of astroglial VEGF in DIO mice prevented obesity-induced hypertension through a reduction in sympathetic hyperactivity directed toward cardiovascular targets. To assess sympathomodulation in cardiovascular regulation, we administered several vasoactive compounds via the carotid artery while measuring heart rate and blood pressure responses simultaneously. While the experimental lowering of blood pressure by infusing intracarotid sodium nitroprusside (SNP; nitric oxide donor) resulted in a similar vasodilation across all experimental groups (Figure S5L), HFHS diet-fed control mice showed a surprising acceleration of the counterregulatory increase in heart rate (baroreflex) relative to SC fed mice; notably, no heart rate differences were observed between HFHS diet versus SC diet-fed shRNA(VEGF)$^{GFAP+}$ mice upon SNP administration (Figure S5L). To further assess how a reduction in astroglial VEGF affects sympathetic modulation of the cardiovascular system, we probed $\beta_{1/2}$-adrenoreceptor function by intracarotid infusion of its pharmacological agonist isoproterenol (50 μg/kg BW). Notably, obese shRNA(VEGF)$^{GFAP+}$ mice retained normal sensitivity toward isoproterenol-mediated stimulation of heart

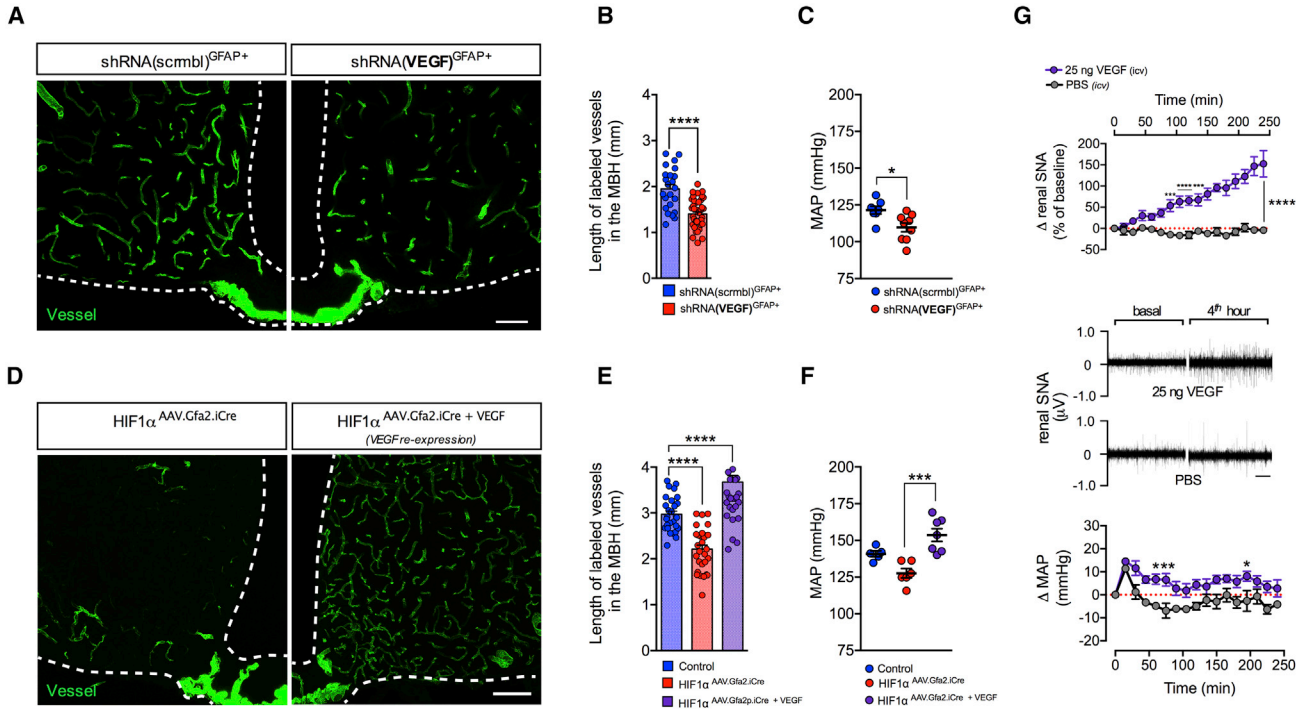

Figure 5. Blocking astroglial VEGF in the MBH protects from hypothalamic angiopathy as well as the development of arterial hypertension in mice upon HFHS diet feeding

(A) Confocal micrographs depicting the vascular profile in the MBH of HFHS-fed mice with astroglial knockdown of VEGF (shRNA(VEGF)$^{GFAP+}$) versus control (scrambled control RNA; shRNA(scrmbl)$^{GFAP+}$). Images are representative of data in (B).

(B) Quantification of labeled vessels in the MBH of HFHS diet-fed shRNA(VEGF)$^{GFAP+}$ versus shRNA(scrmbl)$^{GFAP+}$ mice. n = 4–7 mice per group; 6–8 hemisections/mouse.

(C) Quantification of MAP in a separate cohort of HFHS diet-fed shRNA(VEGF)$^{GFAP+}$ and shRNA(scrmbl)$^{GFAP+}$ mice. Data are represented as a mean MAP of individual mice repeatedly measured over separate days. n = 7–9 mice per group

(D) Confocal micrographs showing the vascular profiles in the MBH of astrocyte-specific HIF1α-deficient mice (HIF1α $^{AAV.Gfa2.iCre}$) compared with astrocyte-specific HIF1α-deficient mice re-expressing VEGF in astrocytes (HIF1α $^{AAV.Gfa2.iCre + VEGF}$) both fed with HFHS diet. Images are representative of data in (E).

(E) Quantification of MBH vessel length in control, HIF1α $^{AAV.Gfa2.iCre}$, and HIF1α $^{AAV.Gfa2.iCre + VEGF}$ mice, all fed with an HFHS diet. n = 5–8 mice per group; 6–8 hemisections/mouse.

(F) Tail-cuff analysis of MAP in a separate cohort of SC diet-fed control, HIF1α $^{AAV.Gfa2.iCre}$, and HIF1α $^{AAV.Gfa2.iCre + VEGF}$ mice. Data are represented as mean MAP of individual mice repeatedly measured over separate days. n = 5–7 mice per group.

(G) Time-resolved assessment of acute changes in renal SNA in anesthetized C57BL/6J mice upon central infusion of VEGF (25 ng; upper panel) with representative neurograms (middle panel; n = 6 mice per group). In a separate cohort, MAP was assessed in conscious mice upon central infusion of VEGF (lower panel; n = 3 mice per group; cross-over design).

Scale bar, 100 μm (A and D). ****p < 0.0001, ***p < 0.001, and *p < 0.05. n.s., not significant. Statistical tests included one-way ANOVA (E and F), two-way ANOVA (G), and unpaired Student's t test (B and C).

rate, whereas obese control mice displayed substantial chronotropic incompetence suggesting myocardial dysfunction such as impaired cardiac contractility or a potential desensitization toward catecholamines due to chronic overstimulation (Figure S5L). While no changes in circulating catecholamines were detected (Figure S5M), though, shRNA(VEGF)$^{GFAP+}$ mice fed with an HFHS diet had an increased expression of β_2-adrenergic receptors in the heart (Figure S5N), potentially underlying the restored contractile responsivity toward isoproterenol upon withdrawal of putative sympathoexcitatory VEGF produced in hypothalamic astrocytes.

Lastly, we further explored the hypothesis that central VEGF may modulate sympathetic outflow acutely by a direct mechanism and thus infused VEGF into the lateral cerebral ventricle (25 ng; i.c.v.) while electrically recording from the postganglionic nerve bundle innervating the kidney. Strikingly, we observed a large and steady increase in renal sympathetic nerve activity (SNA) upon central VEGF infusion as compared with vehicle delivery; central VEGF-induced sympathoexcitation was further accompanied by an acute rise in MAP as measured by radiotelemetry in a separate set of mice following a cross-over design (Figure 5G). Overall, these findings indicate that central VEGF directly increases sympathetic nerve traffic and that conversely, the interference with astroglial VEGF expression that is locally restricted to the MBH prevents the development of HFHS diet-induced arterial hypertension via the abrogation of hyperactive sympathetic outflow toward the cardiovascular system.

HFHS diet feeding, but not hypertension per se, induces hypothalamic angiogenesis in rats

Wondering if hypothalamic angiopathy is potentially primary or solely secondary to elevated blood pressure, we examined a

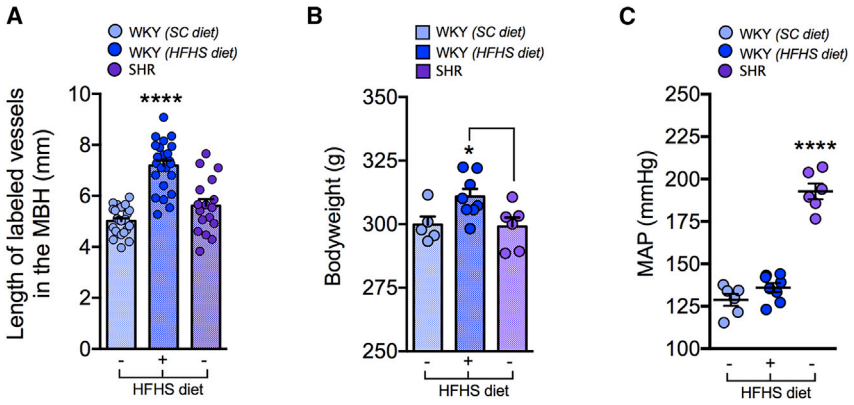

Figure 6. HFHS diet exposure, but not spontaneously developing hypertension, induces hypothalamic microangiopathy in rats

(A) Quantification of hypothalamic vascularity in Wistar Kyoto (WKY) rats fed SC or HFHS diet (4 weeks), or with spontaneously developing hypertension (SHR) under SC diet. Data are presented as mean ± SEM.

(B) Quantification of corresponding terminal bodyweights of WKY rats fed either SC or HFHS diet (4 weeks) as compared with SHR. Data are presented as mean ± SEM.

(C) Quantification of MAP of WKY rats fed either SC or HFHS diet (4 weeks) as compared with SHR as determined by the tail-cuff system measured repeatedly over separate days. Data are presented as mean ± SEM.

****$p < 0.0001$. Statistical tests included one-way ANOVA.

cohort of male Wistar Kyoto (WKY) rats, a subset of which spontaneously develop hypertension on SC diet (Doris, 2017). Despite their dramatically elevated blood pressure, spontaneously hypertensive rats (SHR) showed normal vascularity of the MBH as compared with their normotensive WKY rat littermates (Figures 6A and 6B). Of note, and consistent with our observations in mice, we found that 4 weeks of HFHS diet feeding resulted in a significant hypervascularization response of the rat MBH when arterial blood pressure was not yet increased by the diet (Figures 6B and 6C). In conclusion, we provide evidence that increased vascularity in the hypothalamus is associated with hypertension, which in isolation seems insufficient to trigger hypothalamic vascular remodeling as determined in a hypertensive rat model with diet-independent spontaneous elevations in blood pressure.

DISCUSSION

We have uncovered and characterized an unprecedented involvement of hypothalamic astrocytes in the regulation of systemic blood pressure via a leptin-dependent HIF1α-VEGF mechanism. We initially observed that hypothalamic astrocytes rapidly induce pro-angiogenic HIF1α-VEGF signaling as a consequence of elevated peripheral leptin levels under HFHS diet feeding. This early event during high-calorie exposure was paramount for the initiation of a dynamic astrocyte-dependent hypervascularization response, which proved to be unique to the hypothalamus. The brain-body interface within the MBH is highly susceptible to high-calorie diet exposure and well known to display various cytoarchitectural rearrangements, metabolic disturbances, and pro-inflammatory signaling. Notably, peripheral inflammation, which occurs as a consequence of hypercaloric feeding, for example, in white adipose tissue, has recently been linked to increased HIF1α-VEGF signaling. Importantly, the adipocyte-specific ablation of HIF1α was found to significantly reduce adipose tissue inflammation in mice (Lee et al., 2014), consistent with the improvements we observed in the hypothalamus upon astroglial HIF1α ablation. Analogous to the rapid induction of astroglial VEGF upon high-calorie exposure, a recent report demonstrated an increase of VEGF in the circulation (Jais et al., 2016). In contrast to the pro-angiogenic and permeability-promoting effects of astroglial VEGF (Argaw et al., 2012), the circulating VEGF pool induced by a hypercaloric diet was instead identified as instrumental in a counterregulatory mechanism that restores glucose transport across the cerebral endothelium upon its transient, lipid-induced impairment (Jais et al., 2016; Schüler et al., 2018). These differential downstream effects of VEGF at the cerebral endothelium are likely determined by the site of ligand binding, with blood-borne VEGF acting on endothelial cells from the luminal side as opposed to tissue-produced or parenchymal VEGF which signals to endothelial cells from the abluminal side. Indeed, a previous report delineated the underlying mechanism of differential VEGF signaling, which is specific to neurovascular interfaces and predicated on the polarized apicobasal distribution of endothelial VEGFR-1 (luminal) and VEGFR-2 (abluminal) (Hudson et al., 2014).

Here, we report that HFHS diet feeding triggers the release of VEGF by MBH astrocytes acting on endothelial cells from the parenchymal side. Notably, some tissue-borne VEGF can also stem from tanycytes, which are specialized ependymal cells residing at the third ventricle and previously reported to induce fenestrations in a small subset of specialized vessels in a VEGF-dependent manner upon metabolic challenges (Langlet et al., 2013). While this tanycyte-mediated plasticity appears highly regionalized, phasic by nature, and restricted to a small set of fenestrated vessels, our data here suggest that neighboring astrocytes located deeper within the parenchyma are instead sensitive to more tonic signals reflecting long-term energy status in order to initiate a chronic hypervascularization, barrier impairment, and neuroinflammation. Moreover, we further report that leptin action in the brain is a paramount factor for the development of hypothalamic angiopathy by inducing pro-angiogenic HIF1α-VEGF signaling in local astrocytes. Consistent with this finding, recently emerging evidence suggests that certain cytokines, growth factors, and hormones can modulate HIF1α-VEGF signaling independent of hypoxia (Kietzmann et al., 2016). By engaging different kinase-regulated pathways, these extracellular signals have been shown to result in various phosphorylation events that modify HIF1a signaling either directly or indirectly. Notably, however, mounting evidence suggests that phosphorylation-dependent regulation of HIF signaling may vary greatly depending on the cell type, the

combination of signals, and the physiological context (Kietzmann et al., 2016). Here, for the first time, while we report an evidence suggesting that leptin administration potently induces $pERK_{1/2}$ signaling as well as $LepR_a$-dependent-VEGF induction in MBH astrocytes, the detailed molecular mechanisms involved in coupling leptin signaling with HIF1α-VEGF induction in hypothalamic astrocytes requires further investigations.

Interestingly, a potential link between leptin, VEGF, and the development of vasculopathies has been previously suggested for the retina (Cao et al., 2001; Suganami et al., 2004). In agreement, sparse clinical reports suggest elevations in serum, and particularly vitreal, leptin to independently predict the severity of proliferative diabetic retinopathy in humans (Gariano et al., 2000). Intrigued by these previous reports suggesting that leptin plays a general role in vascular pathobiology, we also assessed the retinal microvasculature in HFHS versus SC diet-fed mice. Even though chronic exposure of C57BL/6J mice to HFHS diet was sufficient to greatly elevate serum leptin levels and induce hypervascularization in the hypothalamus, vascular density remained constant in the retinae of these mice (data not shown). These discrepant results with previous studies may be due to the fact that leptin's pro-angiogenic effects in the retina were studied upon an ischemic stimulus in mice (Suganami et al., 2004) and/or in human subjects with precedent retinopathy (Gariano et al., 2000), each representing highly distinct pathophysiological contexts.

Besides its pro-angiogenic actions at the microvasculature, leptin has also been linked with the development of arterial hypertension and was proposed as an independent factor conferring the obesity-associated risk for cardiovascular mortality. Ample evidence suggests that leptin's effect on cardiovascular regulation is retained in obese individuals, whereas the hormone's capacity to reduce bodyweight and food intake is significantly compromised ("physiologically selective leptin resistance"; reviewed in Mark, 2013). Importantly, the mechanisms by which leptin impacts the cardiovascular system are largely mediated via the central nervous system, particularly through tuning sympathetic outflow from hypothalamic and medullary pre-autonomic nuclei (reviewed in Simonds and Cowley, 2013). Notably, however, recent evidence now suggests that leptin can also act on neural components outside the CNS such as the carotid bodies thereby contributing to sympathoexcitation and hypertension via alternative routes (Caballero-Eraso et al., 2019). Within the CNS, though, the dorsomedial hypothalamus constitutes a region that has gained particular attention for its implications in leptin's hemodynamic and sympathetic effects (Marsh et al., 2003; Simonds et al., 2014). Yet the importance of several other hypothalamic nuclei demands appreciation. Accordingly, considerable evidence has stated that site-specific microinjections of leptin directly into the arcuate nucleus (as part of the MBH) leads to robust increases in sympathetic nerve traffic and a rise in arterial pressure (Rahmouni and Morgan, 2007), while genetic deletion of LepR specifically in this region abrogates these responses (Harlan et al., 2011). While past research was largely focused on the direct—and often transient—effects of leptin on pre-autonomic neurons, we have now extended this model reporting that hypothalamic astrocytes respond to elevations in leptin by chronically increasing HIF1α-VEGF signaling. In turn, increased VEGF seems to promote hyperactivation of the sympathetic nervous system both directly as well as indirectly via chronic remodeling of the gliovascular interface. In light of the immediate pressor and sympathoexcitatory response upon central VEGF administration, central VEGF could trigger direct changes in neuronal excitability and synaptic function of pre-autonomic hypothalamic neurons. Indeed, several reports suggest that VEGF can exert various "non-traditional" functions within the brain that extend beyond the role of a vascular growth and permeabilizing factor, including the acute modulation of neurophysiological properties (Xu et al., 2003; Ma et al., 2009; Huang et al., 2010). On the other hand, our data suggest that VEGF promotes sympathoexcitation via an additional indirect mechanism that involves the chronic remodeling of the gliovascular interface. Here, we propose that by rendering pre-autonomic areas of the hypothalamus more susceptible to pro-inflammatory and pressor-promoting cytokines such as TNF-α (Han et al., 2016), such leptin-VEGF interactions in astrocytes further bias local neurons toward increased SNA in order to promote—and sustain—arterial hypertension in obesity. Sympathetic overdrive as a result of combined neurogenic and gliagenic mechanisms bears severe implications for cardiovascular regulation, including impaired sensitivity of the baroreceptor reflex, an index of arterial baroreceptor function. Contrary to previous reports, however, our studies in DIO mice fed HFHS diet failed to induce impairments in baroreflex sensitivity as assessed in response to blood pressure-lowering or upon administration of the α_1-adrenergic receptor agonist phenylephrine. Importantly, however, most studies investigating baroreflex regulation in the context of obesity were performed in species other than mice, such as in humans (Grassi et al., 1998; Skrapari et al., 2007), dogs (Lohmeier et al., 2016), and rats (McCully et al., 2012), or in obese monogenic mice critically lacking leptin (Hilzendeger et al., 2010) or leptin receptors (Goncalves et al., 2009). In light of leptin's prominent role in enhancing the baroreceptor reflex (Li et al., 2013; Shi et al., 2020), and the fact that endogenous leptin action is retained in DIO at least in mice (Ottaway et al., 2015), further studies are required to elucidate if differences in leptin sensitivity are responsible for the enhanced baroreflex gain we observed in DIO mice.

Conclusions

We propose that exposure to a hypercaloric diet rapidly triggers hypothalamic microangiopathy, a phenomenon that not only occurs prior to and independent of systemic hypertension but also directly contributes to systemic hemodynamic derangements via exaggerated sympathoexcitation. In contrast to other tissues in which elevated capillary pressure has been extensively described as sufficient for triggering renal (Folkow et al., 1958), retinal (Wong et al., 2016), or cortical (de Montgolfier et al., 2019) vascular remodeling, we have found that HFHS diet-induced remodeling of microvascular beds in the hypothalamus is instead primarily driven by hyperleptinemia and predominantly mediated by an intricate gliovascular crosstalk centered at astrocytic VEGF.

In conclusion, here, we highlight the importance of astrocytes for assimilating and integrating the peripheral leptin signal to in turn restructure select hypothalamic microcirculations for

orchestrating long-term elevations in sympathetic outflow and blood pressure.

Limitations of study

The obvious limitation of our study entail a paucity of a more detailed insight into the underlying mechanisms that link astrocytic VEGF with autonomic outflow and blood pressure. This gap in the mechanistic understanding of a gliovascular-to-neuron communication could, for example, be bridged by employing our pharmacological and transgenic mouse models with microendoscopy or fiber-photometry in order to assess pathophysiological changes in astrocytic and neuronal activity within the MBH *in vivo*. Moreover, because of inherent methodological constraints, we report acute, but not longitudinal, analysis of SNA upon central VEGF infusion. Lastly, despite careful acclimatization and handling of mice, a stress-associated effect on tail-cuff blood pressure and serum catecholamines cannot be ruled out entirely.

STAR★METHODS

Detailed methods are provided in the online version of this paper and include the following:

- KEY RESOURCES TABLE
- RESOURCE AVAILABILITY
  - Lead contact
  - Materials availability
  - Data and code availability
- EXPERIMENTAL MODEL AND SUBJECT DETAILS
  - Mouse models
  - Genotyping of mouse lines
  - Rat model
- METHOD DETAILS
  - STZ-induced diabetes mouse model
  - Body composition analysis
  - Measurement of mean arterial pressure in conscious mice by the tail cuff system
  - Arterial pressure and heart rate recording in anesthetized mice
  - Implantation of intracerebroventricular (i.c.v.) cannulation
  - Central VEGF effects in conscious mice with radiotelemetry units
  - Central effects of VEGF on blood pressure, heart rate and renal sympathetic nerve activity in anesthetized mice
  - Leptin administration *in vivo*
  - Glucose metabolism in mice *in vivo*
  - Viral targeting of astrocytic VEGF signaling in the medi-obasal hypothalamus (MBH)
  - *In vivo* bioluminescence imaging of HIF1A/ODD-Luciferase mice
  - *Ex vivo* luciferase assay of HIF1A/ODD-Luc brain homogenates
  - Vascular reactivity experiments in aorta segments
  - Magnetic-activated and fluorescence-assisted cell sorting (MACS/FACS)
  - Fluorescent angiography
  - Assessment of blood-brain barrier integrity
  - Image acquisition and analysis of vascularity in consecutive brain sections
  - Brain sectioning and immunohistochemistry
  - Immunostaining for pSTAT3 and pERK$_{1/2}$
  - Immunostaining for laminin and collagen-IV
  - 3DISCO-assisted optical clearing of whole brains
  - Light-sheet microscopy imaging
  - Analysis of vascularity in 3D whole-brain data sets
  - Analysis of MBH vascularity of consecutive confocal micrographs
  - Analysis of basement membrane thickness
  - Electron microscopy
  - Protein extraction and Western blotting
  - RNA isolation and qPCR analysis
- QUANTIFICATION AND STATISTICAL ANALYSIS

SUPPLEMENTAL INFORMATION

Supplemental information can be found online at https://doi.org/10.1016/j.cmet.2021.04.007.

ACKNOWLEDGMENTS

The authors thank Dr. Nuria Fernández and Dr. Sara Amor for helping with cardiovascular analyses, Stephan Sachs for kindly providing STZ-treated diabetic mice, and Clarita Layritz, Marlene Kilian, Nicole Wiegert, Elisavet Lola, and Cassie Holleman for their excellent technical assistance. This work was supported in part by funding to R.E.C. and P.P. from a Marie Skłodowska-Curie grant (ChroMe # 675610) and M.H.T. and C.G.-C. from the European Research Council (AdG grant Hypoflam # 695054 and STG grant AstroNeuroCrosstalk #757393, respectively), and the German Research Foundation under Germany's Excellence Strategy within the framework of the Munich Cluster for Systems Neurology (EXC 2145 SyNergy – ID 390857198) and Helmholtz Excellence Network. T.D.M. received grant support from the German Research Foundation (SFB TRR152/P23 and SFB TRR296). K.R. is supported by the US National Institutes of Health (HL084207), the Department of Veterans Affairs (merit grant BX004249), the University of Iowa Fraternal Order of Eagles Diabetes Research Center, and the Iowa Neuroscience Institute. T.G. and T.L.H. received support from the Technische Universität München – Institute for Advanced Study, funded by the German Excellence Initiative and the European Union Seventh Framework Programme under grant agreement no. 291763.

AUTHOR CONTRIBUTIONS

T.G., C.G.-C., and M.H.T. conceptualized all studies and designed all experiments. T.G. and C.P. (light-sheet microscopy); R.E.C. (flow-cytometry); T.W. (blood pressure in mice); S.L., C.D.B.M., O.L.T., B.L., and M.H. (metabolic phenotyping); F.J.R.-O. (western blotting); K.S.-B. (electron microscopy); M.G., M.F.-F., A.L.G.-V., and D.G.-H. (blood pressure regulation in mice and rats); A.A.S. and C.A.L. (TRE-Lep^{rtTA} cohort); and D.A.M. (rSNA and radiotelemetry measurements) conducted the experiments and collected and analyzed the data. T.G., C.G.C., and M.H.T. wrote the manuscript in discussion with T.L.H., S.C.W., M.G., C.A.L., K.R., T.D.M., S.U., A.E., C.D.A.S., and P.T.P., who revised the article critically for important intellectual content. All authors have read and approved the final version of the manuscript.

DECLARATION OF INTERESTS

The authors declare no competing interests.

Received: December 10, 2020
Revised: February 27, 2021
Accepted: April 12, 2021
Published: May 4, 2021

REFERENCES

Argaw, A.T., Asp, L., Zhang, J., Navrazhina, K., Pham, T., Mariani, J.N., Mahase, S., Dutta, D.J., Seto, J., Kramer, E.G., et al. (2012). Astrocyte-derived VEGF-A drives blood-brain barrier disruption in CNS inflammatory disease. J. Clin. Invest. *122*, 2454–2468.

Batiuk, M.Y., de Vin, F., Duqué, S.I., Li, C., Saito, T., Saido, T., Fiers, M., Belgard, T.G., and Holt, M.G. (2017). An immunoaffinity-based method for isolating UltraPure adult astrocytes based on ATP1B2 targeting by the ACSA-2 antibody. J. Biol. Chem. *292*, 8874–8891.

Bell, B.B., Harlan, S.M., Morgan, D.A., Guo, D.F., Cui, H., and Rahmouni, K. (2018). Differential contribution of POMC and AgRP neurons to the regulation of regional autonomic nerve activity by leptin. Mol. Metab. *8*, 1–12.

Brenner, M., Kisseberth, W.C., Su, Y., Besnard, F., and Messing, A. (1994). GFAP promoter directs astrocyte-specific expression in transgenic mice. J. Neurosci. *14*, 1030–1037.

Caballero-Eraso, C., Shin, M.K., Pho, H., Kim, L.J., Pichard, L.E., Wu, Z.J., Gu, C., Berger, S., Pham, L., Yeung, H.Y.-.B., et al. (2019). Leptin acts in the carotid bodies to increase minute ventilation during wakefulness and sleep and augment the hypoxic ventilatory response. J. Physiol. *597*, 151–172.

Cao, R., Brakenhielm, E., Wahlestedt, C., Thyberg, J., and Cao, Y. (2001). Leptin induces vascular permeability and synergistically stimulates angiogenesis with FGF-2 and VEGF. Proc. Natl. Acad. Sci. USA *98*, 6390–6395.

De Montgolfier, O., Pinçon, A., Pouliot, P., Gillis, M.-A., Bishop, J., Sled, J.G., Villeneuve, L., Ferland, G., Lévy, B.I., Lesage, F., et al. (2019). High systolic blood pressure induces cerebral microvascular endothelial dysfunction, neurovascular unit damage, and cognitive decline in mice. Hypertension *73*, 217–228.

DeFalco, J., Tomishima, M., Liu, H., Zhao, C., Cai, X., Marth, J.D., Enquist, L., and Friedman, J.M. (2001). Virus-assisted mapping of neural inputs to a feeding center in the hypothalamus. Science *291*, 2608–2613.

Doris, P.A. (2017). Genetics of hypertension: an assessment of progress in the spontaneously hypertensive rat. Physiol. Genomics *49*, 601–617.

Ducy, P., Amling, M., Takeda, S., Priemel, M., Schilling, A.F., Beil, F.T., Shen, J., Vinson, C., Rueger, J.M., and Karsenty, G. (2000). Leptin inhibits bone formation through a hypothalamic relay: a central control of bone mass. Cell *100*, 197–207.

Ertürk, A., Becker, K., Jährling, N., Mauch, C.P., Hojer, C.D., Egen, J.G., Hellal, F., Bradke, F., Sheng, M., and Dodt, H.U. (2012). Three-dimensional imaging of solvent-cleared organs using 3DISCO. Nat. Protoc. *7*, 1983–1995.

Feihl, F., Liaudet, L., Levy, B.I., and Waeber, B. (2008). Hypertension and microvascular remodelling. Cardiovasc. Res. *78*, 274–285.

Flegal, K.M., Kit, B.K., Orpana, H., and Graubard, B.I. (2013). Association of all-cause mortality with overweight and obesity using standard body mass index categories: a systematic review and meta-analysis. JAMA *309*, 71–82.

Folkow, B., Grimby, G., and Thulesius, O. (1958). Adaptive structural changes of the vascular walls in hypertension and their relation to the control of the peripheral resistance. Acta Physiol. Scand. *44*, 255–272.

Franciosi, S., De Gasperi, R., Dickstein, D.L., English, D.F., Rocher, A.B., Janssen, W.G., Christoffel, D., Sosa, M.A., Hof, P.R., Buxbaum, J.D., and Elder, G.A. (2007). Pepsin pretreatment allows collagen IV immunostaining of blood vessels in adult mouse brain. J. Neurosci. Methods *163*, 76–82.

Franklin, K., and Paxinos, G. (2008). The Mouse Brain in Stereotaxic Coordinates, Compact, 3rd Edition. Academic Press.

Gao, Y., Layritz, C., Legutko, B., Eichmann, T.O., Laperrousaz, E., Moullé, V.S., Cruciani-Guglielmacci, C., Magnan, C., Luquet, S., Woods, S.C., et al. (2017). Disruption of lipid uptake in astroglia exacerbates diet-induced obesity. Diabetes *66*, 2555–2563.

García-Cáceres, C., Quarta, C., Varela, L., Gao, Y., Gruber, T., Legutko, B., Jastroch, M., Johansson, P., Ninkovic, J., Yi, C.-X., et al. (2016). Astrocytic insulin signaling couples brain glucose uptake with nutrient availability. Cell *166*, 867–880.

García-Cáceres, C., Balland, E., Prevot, V., Luquet, S., Woods, S.C., Koch, M., Horvath, T.L., Yi, C.X., Chowen, J.A., Verkhratsky, A., et al. (2019). Role of astrocytes, microglia, and tanycytes in brain control of systemic metabolism. Nat. Neurosci. *22*, 7–14.

Gariano, R.F., Nath, A.K., D'Amico, D.J., Lee, T., and Sierra-Honigmann, M.R. (2000). Elevation of vitreous leptin in diabetic retinopathy and retinal detachment. Invest. Ophthalmol. Vis. Sci. *41*, 3576–3581.

Goncalves, A.C.D.C., Tank, J., Diedrich, A., Hilzendeger, A.M., Plehm, R., Bader, M., Luft, F.C., Jordan, J., and Gross, V. (2009). Diabetic hypertensive leptin receptor-deficient db/db mice develop cardioregulatory autonomic dysfunction. Hypertension *53*, 387–392.

Grassi, G., Seravalle, G., Colombo, M., Bolla, G., Cattaneo, B.M., Cavagnini, F., and Mancia, G. (1998). Body weight reduction, sympathetic nerve traffic, and arterial baroreflex in obese normotensive humans. Circulation *97*, 2037–2042.

Haim, L.B., and Rowitch, D.H. (2017). Functional diversity of astrocytes in neural circuit regulation. Nat. Rev. *18*, 31–41.

Han, C., Wu, W., Ale, A., Kim, M.S., and Cai, D. (2016). Central leptin and tumor necrosis factor-α (TNFα) in diurnal control of blood pressure and hypertension. J. Biol. Chem. *291*, 15131–15142.

Harlan, S.M., Morgan, D.A., Agassandian, K., Guo, D.F., Cassell, M.D., Sigmund, C.D., Mark, A.L., and Rahmouni, K. (2011). Ablation of the leptin receptor in the hypothalamic arcuate nucleus abrogates leptin-induced sympathetic activation. Circ. Res. *108*, 808–812.

Hilzendeger, A.M., Goncalves, A.C.D.C., Plehm, R., Diedrich, A., Gross, V., Pesquero, J.B., and Bader, M. (2010). Autonomic dysregulation in ob/ob mice is improved by inhibition of angiotensin-converting enzyme. J. Mol. Med. (Berl) *88*, 383–390.

Hoffmann, A., Bredno, J., Wendland, M., Derugin, N., Ohara, P., and Wintermark, M. (2011). High and low molecular weight fluorescein isothiocyanate (FITC)-dextrans to assess blood-brain barrier disruption: technical considerations. Transl. Stroke Res. *2*, 106–111.

Hoppe, G., Yoon, S., Gopalan, B., Savage, A.R., Brown, R., Case, K., Vasanji, A., Chan, E.R., Silver, R.B., and Sears, J.E. (2016). Comparative systems pharmacology of HIF stabilization in the prevention of retinopathy of prematurity. Proc. Natl. Acad. Sci. USA *113*, E2516–E2525.

Horvath, T.L., Sarman, B., García-Cáceres, C., Enriori, P.J., Sotonyi, P., Shanabrough, M., Borok, E., Argente, J., Chowen, J.A., Perez-Tilve, D., et al. (2010). Synaptic input organization of the melanocortin system predicts diet-induced hypothalamic reactive gliosis and obesity. Proc. Natl. Acad. Sci. USA *107*, 14875–14880.

Hsuchou, H., He, Y., Kastin, A.J., Tu, H., Markadakis, E.N., Rogers, R.C., Fossier, P.B., and Pan, W. (2009). Obesity induces functional astrocytic leptin receptors in hypothalamus. Brain *132*, 889–902.

Huang, Y.F., Yang, C.H., Huang, C.C., Tai, M.H., and Hsu, K.S. (2010). Pharmacological and genetic accumulation of hypoxia-inducible factor-1 alpha enhances excitatory synaptic transmission in hippocampal neurons through the production of vascular endothelial growth factor. J. Neurosci. *30*, 6080–6093.

Hudson, N., Powner, M.B., Sarker, M.H., Burgoyne, T., Campbell, M., Ockrim, Z.K., Martinelli, R., Futter, C.E., Grant, M.B., Fraser, P.A., et al. (2014). Differential apicobasal VEGF signaling at vascular blood-neural barriers. Dev. Cell *30*, 541–552.

Jais, A., Solas, M., Backes, H., Chaurasia, B., Kleinridders, A., Theurich, S., Mauer, J., Steculorum, S.M., Hampel, B., Goldau, J., et al. (2016). Myeloid-cell-derived VEGF maintains brain glucose uptake and limits cognitive impairment in obesity. Cell *165*, 882–895.

Kantzer, C.G., Boutin, C., Herzig, I.D., Wittwer, C., Reiß, S., Tiveron, M.C., Drewes, J., Rockel, T.D., Ohlig, S., Ninkovic, J., et al. (2017). Anti-ACSA-2 defines a novel monoclonal antibody for prospective isolation of living neonatal and adult astrocytes. Glia *65*, 990–1004.

Kietzmann, T., Mennerich, D., and Dimova, E.Y. (2016). Hypoxia-inducible factors (HIFs) and phosphorylation: impact on stability, localization, and transactivity. Front. Cell Dev. Biol. *4*, 11.

Kim, J.G., Suyama, S., Koch, M., Jin, S., Argente-Arizon, P., Argente, J., Liu, Z.W., Zimmer, M.R., Jeong, J.K., Szigeti-Buck, K., et al. (2014). Leptin

signaling in astrocytes regulates hypothalamic neuronal circuits and feeding. Nat. Neurosci. *17*, 908–910.

Langlet, F., Levin, B.E., Luquet, S., Mazzone, M., Messina, A., Dunn-Meynell, A.A., Balland, E., Lacombe, A., Mazur, D., Carmeliet, P., et al. (2013). Tanycytic VEGF-A boosts blood-hypothalamus barrier plasticity and access of metabolic signals to the arcuate nucleus in response to fasting. Cell Metab *17*, 607–617.

Lee, Y.S., Kim, J.W., Osborne, O., Oh, D.Y., Sasik, R., Schenk, S., Chen, A., Chung, H., Murphy, A., Watkins, S.M., et al. (2014). Increased adipocyte O2 consumption triggers HIF-1α, causing inflammation and insulin resistance in obesity. Cell *157*, 1339–1352.

Li, B., Shi, Z., Cassaglia, P.A., and Brooks, V.L. (2013). Leptin acts in the forebrain to differentially influence baroreflex control of lumbar, renal, and splanchnic sympathetic nerve activity and heart rate. Hypertension *61*, 812–819.

Lohmeier, T.E., Iliescu, R., Tudorancea, I., Cazan, R., Cates, A.W., Georgakopoulos, D., and Irwin, E.D. (2016). Chronic interactions between carotid baroreceptors and chemoreceptors in obesity hypertension. Hypertension *68*, 227–235.

Ma, Y.Y., Li, K.Y., Wang, J.J., Huang, Y.L., Huang, Y., and Sun, F.Y. (2009). Vascular endothelial growth factor acutely reduces calcium influx via inhibition of the Ca2+ channels in rat hippocampal neurons. J. Neurosci. Res. *87*, 393–402.

Madisen, L., Zwingman, T.A., Sunkin, S.M., Oh, S.W., Zariwala, H.A., Gu, H., Ng, L.L., Palmiter, R.D., Hawrylycz, M.J., Jones, A.R., et al. (2010). A robust and high-throughput Cre reporting and characterization system for the whole mouse brain. Nat. Neurosci. *13*, 133–140.

Mark, A.L. (2013). Selective leptin resistance revisited. Am. J. Physiol. Regul. Integr. Comp. Physiol. *305*, R566–R581.

Marsh, A.J., Fontes, M.A.P., Killinger, S., Pawlak, D.B., Polson, J.W., and Dampney, R.A.L. (2003). Cardiovascular responses evoked by leptin acting on neurons in the ventromedial and dorsomedial hypothalamus. Hypertension *42*, 488–493.

Mathiisen, T.M., Lehre, K.P., Danbolt, N.C., and Ottersen, O.P. (2010). The perivascular astroglial sheath provides a complete covering of the brain microvessels: an electron microscopic 3D reconstruction. Glia *58*, 1094–1103.

Matthews, D.R., Hosker, J.P., Rudenski, A.S., Naylor, B.A., Treacher, D.F., and Turner, R.C. (1985). Homeostasis model assessment: insulin resistance and beta-cell function from fasting plasma glucose and insulin concentrations in man. Diabetologia *28*, 412–419.

McCully, B.H., Brooks, V.L., and Andresen, M.C. (2012). Diet-induced obesity severely impairs myelinated aortic baroreceptor reflex responses. Am. J. Physiol. Heart Circ. Physiol. *302*, H2083–H2091.

McMinn, J.E., Liu, S.-M., Liu, H., Dragatsis, I., Dietrich, P., Ludwig, T., Boozer, C.N., and Chua, C.S., Jr. (2005). Neuronal deletion of Lepr elicits diabesity in mice without affecting cold tolerance or fertility. Am J Physiol Endocrinol Metab *289*, 403–411.

Mori, T., Tanaka, K., Buffo, A., Wurst, W., Kühn, R., and Götz, M. (2006). Inducible gene deletion in astroglia and radial glia–a valuable tool for functional and lineage analysis. Glia *54*, 21–34.

Oishi, J.C., Castro, C.A., Silva, K.A., Fabricio, V., Cárnio, E.C., Phillips, S.A., de Duarte, A.C.G.O., and Rodrigues, G.J. (2018). Endothelial dysfunction and inflammation precedes elevations in blood pressure induced by a high-fat diet. Arq. Bras. Cardiol. *110*, 558–567.

Ottaway, N., Mahbod, P., Rivero, B., Norman, L.A., Gertler, A., D'Alessio, D.A., and Perez-Tilve, D. (2015). Diet-induced obese mice retain endogenous leptin action. Cell Metab *21*, 877–882.

Pekny, M., Levéen, P., Pekna, M., Eliasson, C., Berthold, C.H., Westermark, B., and Betsholtz, C. (1995). Mice lacking glial fibrillary acidic protein display astrocytes devoid of intermediate filaments but develop and reproduce normally. EMBO J *14*, 1590–1598.

Poirier, P., Giles, T.D., Bray, G.A., Hong, Y., Stern, J.S., Pi-Sunyer, F.X., and Eckel, R.H.; American Heart Association, and Obesity Committee of the Council on Nutrition, Physical Activity, and Metabolism (2006). Obesity and cardiovascular disease: pathophysiology, evaluation, and effect of weight loss: an update of the 1997 American Heart Association Scientific Statement on Obesity and Heart Disease from the Obesity Committee of the Council on Nutrition, Physical Activity, and Metabolism. Circulation *113*, 898–918.

Rahmouni, K., and Morgan, D.A. (2007). Hypothalamic arcuate nucleus mediates the sympathetic and arterial pressure responses to leptin. Hypertension *49*, 647–652.

Rask-Madsen, C., and King, G.L. (2013). Vascular complications of diabetes: mechanisms of injury and protective factors. Cell Metab *17*, 20–33.

Roggendorf, W., Opitz, H., and Schuppan, D. (1988). Altered expression of collagen type VI in brain vessels of patients with chronic hypertension. A comparison with the distribution of collagen IV and procollagen III. Acta Neuropathol *77*, 55–60.

Ryan, H.E., Poloni, M., McNulty, W., Elson, D., Gassmann, M., Arbeit, J.M., and Johnson, R.S. (2000). Hypoxia-inducible factor-1alpha is a positive factor in solid tumor growth. Cancer Res. *60*, 4010–4015.

Safran, M., Kim, W.Y., O'Connell, F., Flippin, L., Günzler, V., Horner, J.W., DePinho, R.A., and Kaelin, W.G. (2006). Mouse model for noninvasive imaging of HIF prolyl hydroxylase activity: assessment of an oral agent that stimulates erythropoietin production. Proc. Natl. Acad. Sci. USA *103*, 105–110.

Sato, S., Hanada, R., Kimura, A., Abe, T., Matsumoto, T., Iwasaki, M., Inose, H., Ida, T., Mieda, M., Takeuchi, Y., et al. (2007). Central control of bone remodeling by neuromedn U. Nat Med *13*, 1234–1240.

Schüler, R., Seebeck, N., Osterhoff, M.A., Witte, V., Flöel, A., Busjahn, A., Jais, A., Brüning, J.C., Frahnow, T., Kabisch, S., et al. (2018). VEGF and GLUT1 are highly heritable, inversely correlated and affected by dietary fat intake: consequences for cognitive function in humans. Mol. Metab. *11*, 129–136.

Shi, Z., Pelletier, N.E., Wong, J., Li, B., Sdrulla, A.D., Madden, C.J., Marks, D.L., and Brooks, V.L. (2020). Leptin increases sympathetic nerve activity via induction of its own receptor in the paraventricular nucleus. eLife *9*, e55357.

Simonds, S.E., and Cowley, M.A. (2013). Hypertension in obesity: is leptin the culprit? Trends Neurosci *36*, 121–132.

Simonds, S.E., Pryor, J.T., Ravussin, E., Greenway, F.L., Dileone, R., Allen, A.M., Bassi, J., Elmquist, J.K., Keogh, J.M., Henning, E., et al. (2014). Leptin mediates the increase in blood pressure associated with obesity. Cell *159*, 1404–1416.

Skowronski, A.A., LeDuc, C.A., Foo, K.S., Goffer, Y., Burnett, L.C., Egli, D., and Leibel, R.L. (2020). Physiological consequences of transient hyperleptinemia during discrete developmental periods on body weight in mice. Sci. Transl. Med. *12*, eaax6629.

Skrapari, I., Tentolouris, N., Perrea, D., Bakoyiannis, C., Papazafiropoulou, A., and Katsilambros, N. (2007). Baroreflex sensitivity in obesity: relationship with cardiac autonomic nervous system activity. Obesity (Silver Spring) *15*, 1685–1693.

Suganami, E., Takagi, H., Ohashi, H., Suzuma, K., Suzuma, I., Oh, H., Watanabe, D., Ojima, T., Suganami, T., Fujio, Y., et al. (2004). Leptin stimulates ischemia-induced retinal neovascularization: possible role of vascular endothelial growth factor expressed in retinal endothelial cells. Diabetes *53*, 2443–2448.

Ternacle, J., Wan, F., Sawaki, D., Surenaud, M., Pini, M., Mercedes, R., Ernande, L., Audureau, E., Dubois-Rande, J.L., Adnot, S., et al. (2017). Short-term high-fat diet compromises myocardial function: a radial strain rate imaging study. Eur. Heart J. Cardiovasc. Imaging *18*, 1283–1291.

Thaler, J.P., Yi, C.X., Schur, E.A., Guyenet, S.J., Hwang, B.H., Dietrich, M.O., Zhao, X., Sarruf, D.A., Izgur, V., Maravilla, K.R., et al. (2012). Obesity is associated with hypothalamic injury in rodents and humans. J. Clin. Invest. *122*, 153–162.

Tsilibary, E.C. (2003). Microvascular basement membranes in diabetes mellitus. J. Pathol. *200*, 537–546.

Williams, L.M., Campbell, F.M., Drew, J.E., Koch, C., Hoggard, N., Rees, W.D., Kamolrat, T., Thi Ngo, H., Steffensen, I.L., Gray, S.R., and Tups, A. (2014). The development of diet-induced obesity and glucose intolerance in C57BL/6 mice on a high-fat diet consists of distinct phases. PLoS One *9*, e106159.

Wong, T.Y., Cheung, C.M., Larsen, M., Sharma, S., and Simó, R. (2016). Diabetic retinopathy. Nat. Rev. Dis. Primers *2*, 16012.

Xu, J.Y., Zheng, P., Shen, D.H., Yang, S.Z., Zhang, L.M., Huang, Y.L., and Sun, F.Y. (2003). Vascular endothelial growth factor inhibits outward delayed-rectifier potassium currents in acutely isolated hippocampal neurons. Neuroscience *118*, 59–67.

Yi, C.X., Gericke, M., Krüger, M., Alkemade, A., Kabra, D.G., Hanske, S., Filosa, J., Pfluger, P., Bingham, N., Woods, S.C., et al. (2012). High calorie diet triggers hypothalamic angiopathy. Mol. Metab. *1*, 95–100.

STAR★METHODS

KEY RESOURCES TABLE

REAGENT or RESOURCE	SOURCE	IDENTIFIER
Antibodies		
Rat anti-ACSA-2	Milteny	130-097-678
Sheep anti-albumin	Abcam	Cat# ab8940; RRID: AB_306875
Mouse anti-claudin-5	Life technology	Cat# 35-2500; RRID: AB_2533200
Goat anti-collagen IV	Chemicon/Merck	Cat# AB769; RRID: AB_11210995
Rabbit anti-phospho-p44/42 MAPK/ERK1/2) (Thr202/Tyr204)	Cell Signaling Technology	Cat# 9101; RRID: AB_331646
Goat anti-GFAP	Dako	Cat# Z0334; RRID: AB_10013382
Chicken anti-GFP	Abcam	Cat# ab13970; RRID: AB_300798
Rabbit anti-HIF-1α	Abcam	Cat# ab82832; RRID: AB_1860665
Goat anti-Iba1	Synaptic Systems	Cat# 234 003; RRID: AB_10641962
Anti-Ki67	Abcam	Cat# ab16667; RRID: AB_302459
Rabbit anti-laminin	Dako	Cat# Z0097; RRID: AB_2313665
Mouse anti-NeuN	Merck	Cat# MAB377; RRID: AB_2298772
Rabbit anti-phospho-STAT3 (Tyr705) (D3A7)	Cell Signaling Technology	Cat# 9145; RRID: AB_2491009
Rabbit anti-VEGF (A-20)	Santa Cruz	Cat# sc-152; RRID: AB_2212984
Mouse anti-β-actin (AC-15) (HRP)	Abcam	Cat# ab49900; RRID: AB_867494
Alexa Fluor 488 goat anti-chicken IgG	Invitrogen	Cat# A-11039; RRID: AB_142924
Alexa Fluor 647 donkey anti-goat IgG	Invitrogen	Cat# A-21447; RRID: AB_141844
Alexa Fluor 405 goat anti-mouse IgG	Invitrogen	Cat# A-31553; RRID: AB_221604
Alexa Fluor 568 donkey anti-rabbit IgG	Invitrogen	Cat# A10042; RRID: AB_2534017
Alexa Fluor 647 donkey anti-rabbit IgG	Invitrogen	Cat# A-31573; RRID: AB_2536183
Alexa Fluor 647 donkey anti-sheep IgG	Invitrogen	Cat# A21448; RRID: AB_1500712
Chemicals, peptides, and recombinant proteins		
Acetylcholine	Sigma-Aldrich	A6625
Benzyl alcohol	Sigma-Aldrich	24122-1L
Benzyl benzoate	Sigma-Aldrich	B6630-250ML
Cobalt (II) chloride hexahydrate	Sigma-Aldrich	C8661-25G
Dichloromethane	Sigma-Aldrich	270997-100ML
Doxycycline hyclate	Sigma-Aldrich	D9891
Durcupan	Electron Microscopy Sciences	14040
Formvar	Electron Microscopy Sciences	15800
Gelatin from porcine skin (SUMI)	VWR International	SAFSG1890
Glutaraldehyde	Electron Microscopy Sciences	16316
Heparin	Sigma-Aldrich	H0200000
Isoproterenol	Sigma-Aldrich	I-5627
KCl	Sigma-Aldrich	P9541
MTBE	Sigma-Aldrich	1634-04-4
NuPAGE LDS sample buffer (4x)	Novex/Life Technologies	NP008
Osmium Tetroxide	Electron Microscopy Sciences	19150
Paraformaldehyde	Carl Roth	0335.2
Pepsin	DAKO/Agilent	S3002
Primers	Thermo Fisher	N/A
Recombinant mouse leptin	R&D systems	498-OB

(*Continued on next page*)

Continued

REAGENT or RESOURCE	SOURCE	IDENTIFIER
Recombinant Mouse VEGF164	R&D systems	493-MV
Skim milk powder	Sigma-Aldrich	70166-500 g
Sodium nitroprusside	Sigma-Aldrich	1614501
Tamoxifen	Sigma-Aldrich	T5648-1g
TaqMan Gene Expression Assay	Thermo Fisher	N/A
TaqMan Universal Master Mix II, no UNG	Thermo Fisher	4440040
Tetrahydrofuran	Sigma-Aldrich	186562-1L
Thromboxane A2 U46619	Sigma-Aldrich	CAS 56985-40-1
Triton X-100	Roche Diagnostics	11858620
Tween-20	Sigma-Aldrich	9005-64-5
Critical commercial assays		
Adult Brain Dissociation	Milteny	130-107-677
Bright-Glo Luciferase Assay System	Promega	E2610
Mouse/Rat Leptin ELISA	Alpco	22-LEPMS-E01
Pierce BCA protein assay	Thermo Fisher	23228
QuickDetect catecholamine (mouse) ELISA Kit	Enzo Lifesciences	E4462
RNeasy Micro Kit	QUIAGEN	74004
RNeasy Mini Kit	QUIAGEN	74104
SMARTer PCR cDNA synthesis kit	TaKaRa	634455
Experimental models: Organisms/strains		
Mouse $Lep^{ob/ob}$	Jackson Laboratory	B6.Cg-Lepob/J;BKS.Cg-Dock7m+/+
Mouse $Lep^{db/db}$	Jackson Laboratory	Leprdb/J; Maine, USA
Mouse TRE-Lep^{rtTA}	Dr. LeDuc; Columbia University; USA (Skowronski et al., 2020)	N/A
Mouse $LepR_b$:Ai14	This paper	B6.129(Cg)-LepRtm(cre)Rck/J;B6.Cg-Gt(ROSA)26Sortm14(CAGtdTomato)Hze/J
Mouse $LepR^{i\Delta astro/GFAP+}$	Kim et al., 2014	B6.129P2-Leprtm1Rck/J;B6.Cg-Tg(GFAPcre/ERT2)505Fmv/J
Mouse HIF-1$\alpha^{i\Delta astro/GFAP+}$	This paper	B6.129-Hif1atm3Rsjo/J;B6.Cg-Tg(GFAPcre/ERT2)505Fmv/J
Mouse HIF-1$\alpha^{i\Delta astro/GLAST+}$	This paper	B6.129-Hif1atm3Rsjo/J;Slc1a3$^{tm1(cre/ERT2)Mgoe}$
Mouse HIF1/ODD-Luciferase	Jackson Laboratory	FVB.129S6-Gt(ROSA)26Sortm2(HIF1A/luc)Keal/Js
Mouse hGFAP.CreER^{T2}	Dr. Vaccarino; Yale University; USA	B6.Cg-Tg(GFAPcre/ERT2)505Fmv/J
Mouse GLAST.CreER^{T2}	Prof. Goetz; LMU/HMGU Munich; GER	Slc1a3$^{tm1(cre/ERT2)Mgoe}$
Mouse ROSA26 mT/mG	Jackson Laboratory	B6.129(Cg)-*Gt(ROSA)26Sor*$^{tm4(ACTB-tdTomato,-EGFP)Luo}$/J
Rat Wistar Kyoto	Envigo	WKY/NHsd
Rat SHR (spontaneous hypertensive rat)	Envigo	SHR/NHsd
Oligonucleotides		
VEGF shRNA targeting sequence 5′ -*TGA AGA TGT ACT CTA TCT CGT*-3′	Vector Biolabs	Nt 1218-1238 of NM_009505
Hairpin loop sequence 5′ -GTT TTG GCC ACT GAC TGAC-3′	Vector Biolabs	N/A
$VEGF_{164}$ overexpressing sequence	Vector Biolabs	RefSeq#:BC061468
$LepR_a$ forward primer 5′ -GAA GTC TCT CAT GAC CAC TAC AGA TGA-3′	Sigma-Aldrich	N/A
$LepR_a$ reverse primer 5′ - TTG TTT CCC TCC ATC AAA ATG TAA -3′	Sigma-Aldrich	N/A

(*Continued on next page*)

Continued

REAGENT or RESOURCE	SOURCE	IDENTIFIER
$LepR_b$ forward primer 5′ - GCA TGC AGA ATC AGT GAT ATT TGG-3′	Sigma-Aldrich	N/A
$LepR_b$ reverse primer 5′ - CAA GCT GTA TCG ACA CTG ATT TC TTC -3′	Sigma-Aldrich	N/A
Software and algorithms		
FIJI	NIH	https://imagej.net/Fiji/Downloads
FlowJo	BD	N/A
GraphPad Prism 6.0 h	GraphPad Software	N/A
IMARIS x64 9.1.2	Oxford instruments	N/A
MacLab Chart Pro 7.0	GE Healthcare	N/A
Other		
Bovine serum albumin	Sigma Aldrich	A8806
Gelatin from porcine skin (SUMI)	VWR International	SAFSG1890
Glo Lysis Buffer	Promega	E2661
Halt protease and phosphatase inhibitors (100x)	Thermo Fisher Scientific, Waltham, USA	78446
Radioimmunoprecipitation assay (RIPA) buffer	Sigma-Aldrich	R0278-500ML
AAV.Gfa2.iCre	Vector Biolabs	Cat. No.: VB1172
AAV.Gfa2.$VEGF_{GFP}$	Vector Biolabs	Cat. No.: AAV-275992
AAV.Gfa2.EGFP	Vector Biolabs	Cat. No.: VB1180
Lectin-FITC conjugate	Thermo Fisher	L4895
WGA-Alexa Fluor 647	Thermo Fisher	W32466
NeuroTrace 435/455	Thermo Fisher	N21479
NeuroTrace 500/525	Thermo Fisher	N21480
Albumin FITC	Sigma Aldrich	A9771
Dextran-FITC (40 kDa)	Sigma Aldrich	Cat# 53379

RESOURCE AVAILABILITY

Lead contact

Request for further information, reagents and resources should be directed and will be fulfilled by the Lead Contact, Cristina García-Cacéres (garcia-caceres@helmholtz-muenchen.de).

Materials availability

Mouse lines (HIF1α::hGFAP.CreER^{T2}; HIF1α::hGLAST.CreER^{T2}; LepR::hGFAP.CreER^{T2}) and AAV vectors (*e.g.* Gfa2.shRNA(VEGF/scrmbl, Gfa2.VEGF.GFP over expressing, etc.) generated in this study are available from the lead contact upon request.

Data and code availability

Not applicable.

EXPERIMENTAL MODEL AND SUBJECT DETAILS

Mouse models

Mouse studies were approved by the Animal Ethics Committee of the government of Upper Bavaria (Germany), the Yale University School of Medicine (CT, US), Medicine Faculty of Universidad Autónoma de Madrid (Spain) and the University of Iowa (IA, UA). Wild-type mice (C57BL/6J, Janvier, Le Genest-Saint-Isle, France) or genetically modified mice aged 12 weeks were provided *ad libitum* access to either a pelleted standard chow (SC) diet (5.6% fat; LM-485, Harlan Teklad) or a high-fat, high-sucrose (HFHS) diet (D12331; 58% of calories from lipids; Research Diets, New Brunswick, NJ). Animals had continuous free access to water and were maintained at 23°C with constant humidity on a 12-h light–dark cycle. Lep$^{ob/ob}$ mice and Lep$^{db/db}$ mice were originally provided from Jackson Laboratory (strain name: B6.Cg-Lepob/J; BKS.Cg-Dock7m +/+ Leprdb/J; Maine, USA). Leptin-overexpressing mice (TRE-Lep ^{rtTA}) were generated from KH2 embryonic stem cell line to include M2rtTA at the Rosa26 locus and the mouse *Lep* gene with tetracycline-response element (TRE) upstream (TRE-Lep) as described previously (Skowronski et al., 2020). Study animals were bred

by crossing homozygous TRE-Lep females with heterozygous ROSA26^{rtTA} males to generate 50% of TRE-Lep^{rtTA}, which induce leptin production when exposed to doxycycline (DOX), and 50% TRE-Lep control littermates unresponsive to doxycycline (DOX). 200 μg/ml of DOX was administered to a cohort of 14-week-old male and female mice in their drinking water for 4 weeks. For visualization of the expression pattern of the long-form leptin receptor the LepR$_b$:Ai14 reporter mouse model was employed, which was derived from inter-crossing LepR$_b$-Cre mice (DeFalco et al., 2001) and Ai14 mice (Madisen et al., 2010) both provided from Jackson Laboratory (strain name: B6.129(Cg)-LepRtm(cre)Rck/J and B6.Cg-Gt(ROSA)26Sortm14(CAG-tdTomato)Hze/J, respectively). LepR $^{loxP/loxP}$ mice (McMinn et al., 2005), HIF1α $^{loxP/loxP}$ mice (Ryan et al., 2000) as well as HIF1/ODD-Luciferase mice (Safran et al., 2006) were generated and described previously and provided from Jackson Laboratory (strain name: B6.129-Hif1atm3Rsjo/J, B6.129P2-Leprtm1Rck/J and FVB.129S6-Gt(ROSA)26Sortm2(HIF1A/luc)Keal/J, respectively). In order to generally excise sequences flanked by loxP sites, mice were crossed with one of the astrocyte-specific CreER^{T2}-driver lines: (1) the transgenic hGFAP-CreER^{T2} mouse line, which was generated on a C57BL/6J background and provided by F.M. Vaccarino (Yale University, School of Medicine, CT, US), or (2) the GLAST.CreER^{T2} mouse line in which Cre recombinase is knocked into the locus of the GLAST gene (Mori et al., 2006). All experiments using the GLAST-specific driver mice were performed with the GLAST.CreERT2 allele in heterozygosity. In both inducible models, nuclear translocation and hence activation of CreER^{T2} was induced postnatally in 6-week-old mice by repeated injections of Tamoxifen (10 mg/kg BW; i.p.) for 5 consecutive days. Tamoxifen (Sigma) was dissolved in sunflower oil at a final concentration of 10 mg/ml at 37°C and filter sterilized. Whenever indicated, mice were further backcrossed to the Cre-dependent reporter mouse line ROSA26 mT/mG provided from Jackson Laboratory (strain name: mT/mG) in order to identify recombined cells by means of membrane-localized EGFP expression. As described previously, GFAP-CreER^{T2} driver mice displayed extensive recombination in thalamic and hypothalamic regions with poor cortical recombination, while GLAST.CreER^{T2} mice displayed extensive recombination in all brain regions except for thalamic nuclei (García-Cáceres et al., 2016). All mice used in experiments displayed good general health. C57BL/6J wildtype mice (Janvier) as well as Lep$^{ob/ob}$ mice and Lep$^{db/db}$ mice (Jackson Laboratory) were purchased and immediately entered experiments upon sufficient acclimatization to the facility. The remaining genetically modified mice were generated and maintained as in-house colonies. While both sexes were included for the study of TRE-Lep^{rtTA} mouse model, the remaining experiments were conducted in exclusively male littermates.

Genotyping of mouse lines

Eartags were obtained from mice at the age of 3 weeks and DNA was isolated by boiling the eartags for 30 min in 200 μl 50 mM NaOH at 95°C (ThermoMixer C, Eppendorf). Afterwards, 20 μl 1 M Tris was added to normalize the pH. 2 μl of isolated genomic DNA was used for the genotyping PCR (Promega) using respective protocols.

Rat model

Rat studies were approved by the Animal Ethics Committee of the government of Universidad Autónoma de Madrid (Spain). Spontaneously hypertensive rats (SHR) and Wistar Kyoto (WKY) rats (Envigo; Indianapolis; USA) were group housed with continuous free access to pelleted food and water and were maintained at 23°C with constant humidity on a 12-h light–dark cycle. All rats used in experiments were directly purchased (Envigo), displayed good general health and immediately entered experiments upon sufficient acclimatization to the facility. Hypothalamic vascular profiles were assessed in 16-week-old male WKY rats either fed 4 weeks HFHS diet (D12331; 58% of calories from lipids; Research Diets, New Brunswick, NJ) or SC diet and compared to littermates with spontaneously hypertensive rats (SHR) maintained on SC diet. Bodyweight was assessed repeatedly as well as blood pressure using tail cuff measurements conducted over the course of four consecutive days (Niprem 645 blood pressure system; Cibertec, Madrid, Spain). At the day of sacrifice, rats received 10 ml/kg of FITC-albumin (10 mg/ml in 0.9% NaCl; MW 69 kDa, Merck, Germany) via the tail vein. After circulation of the tracer for 5 min, rats were decapitated, blood was collected for determining circulating leptin levels and brains were rapidly immersion-fixed in 4% PFA in 0.1 M PBS (pH 7.4) for 72 h at 4°C.

METHOD DETAILS

STZ-induced diabetes mouse model

Insulin-dependent diabetes mellitus was experimentally induced by administering the β-cell toxin Streptozotocin (STZ) to 8-week-old, male wild-type mice (C57BL/6J) according to the multiple low-dose injection protocol of the Diabetic Complications Consortium (50 mg/kg BW; i.p for 5 days versus vehicle (Na-Citrate Buffer)). One group received daily injections of polyethylene-glycosylated (PEGylated)-insulin (25 nmol/kg/day in 5 μl/g) to achieve normoglycemia. PEGylated insulin was synthesized by N-terminal amine reductive amination with 20K methoxy PEG propionaldehyde. In brief, human insulin was dissolved in 50 mM sodium acetate buffer (pH 5.0) and 50% acetonitrile. A 30-fold excess of sodium cyanoborohydride and a 1.5-fold excess of methoxy PEG propionaldehyde (M-ALD-20K, JenKem Technology USA, Plano, TX) was added to the insulin-containing buffer for 3 h at room temperature with stirring. Purification by reverse phase chromatography on a C-8 column in 0.1% TFA acetonitrile solvents yielded PEGylated insulin at greater than 95% purity.

Body composition analysis

Body composition (fat and lean mass) was assessed by using a magnetic resonance whole-body composition analyzer (Echo-MRI, Houston, TX).

Measurement of mean arterial pressure in conscious mice by the tail cuff system

Mean arterial blood pressure (MAP) measurements were performed in each mouse every other day for two weeks before sacrifice by tail-cuff plethysmography using either a Niprem 645 blood pressure system (Cibertec, Madrid, Spain) or a Hatteras MC4000 multi-channel blood pressure analysis system (Hatteras, North Carolina, USA). For that purpose, mice were placed in a quiet area (22±2°C) and habituated to the experimental conditions for at least 3 days. Before measurements, mice were pre-warmed to 34°C for 10–15 min. Then, the occlusion cuff was placed at the base of the tail and the sensor cuff was placed next to the occlusion cuff. Next, the occlusion cuff was inflated to 250 mm Hg and deflated over 20 s. Five to six measurements were recorded in each mouse and the mean of all measurements was calculated each day per animal.

Arterial pressure and heart rate recording in anesthetized mice

Mice were anesthetized with a mixture of ketamine (70 mg/kg) and xylazine (5 mg/kg). Afterwards, the throat was incised from below the mandible to the thoracic inlet. Under a dissecting microscope, the left carotid artery was exposed and carefully separated from other neighboring structures including the vagus nerve. After left carotid isolation, a silk suture (6-0) was placed distally for the complete ligation of the vessel. Then the left carotid artery was proximally occluded with a clamp to produce temporary obstruction of blood flow. Afterwards a small incision was made to insert a polyethylene tube filled with saline containing 100 units heparin/ml. The polyethylene tube had two branches; one for the injection of drugs and the other one with a lateral connection in the perfusion cannula connected to a pressure transducer (Statham Instruments, Los Angeles, CA, US). Mean arterial blood pressure was recorded using the PowerLab/8e data acquisition system (ADInstruments, Colorado Springs, CO, US), and the heart rate was obtained from the arterial pressure recording. The baroreflex control of the heart rate was assessed by administering a bolus of sodium nitroprusside (SNP; 500 μg/kg BW). The α-adrenergic sensitivity was assessed by measuring the changes in mean blood pressure (MBP) after phenylephrine carotid infusion (PE; 50 μg/kg BW) and the β-adrenergic sensitivity was assessed by measuring the changes in both MBP and heart rate to isoproterenol carotid administration (IPR; 50 μg/kg BW).

Implantation of intracerebroventricular (i.c.v.) cannulation

C57BL/6J mice were anesthetized with isoflurane (5% for induction; 1-2% to sustain). Once anesthetized, each mouse was placed in a stereotaxic device and implanted with a stainless-steel cannula (25G, 9 mm length) into the lateral brain ventricle (0.3 mm posterior and 1.0 mm lateral to bregma and 3.0 mm below the surface of the skull) as described previously (Bell et al., 2018). Mice were allowed to recover for 7-10 days. Cannula-implanted mice were either selected for implantation of a radiotelemetry unit (see below) or for the acute effects of VEGF (i.c.v.) versus vehicle (PBS) on blood pressure (BP), heart rate (HR) and renal sympathetic nerve activity (rSNA) in the anesthetized mouse.

Central VEGF effects in conscious mice with radiotelemetry units

Blood pressure (BP) and heart rate (HR) were monitored in conscious, unrestrained mice with an implantable radio-telemetry device (TA11PA-C10, Data Science International). Under isoflurane anesthesia (5% for induction; 1-2% to sustain) and aseptic surgical conditions, a radio-telemetric catheter was implanted into the left common carotid artery through a ventral neck incision. The transmitter unit was placed in a sub-cutaneous pocket located on the right flank below the ribs. After 10-12 days of recovery, direct BP and HR were continuously measured in a conscious, unrestrained mouse with the use of a single-unit telemetry acquisition device (R11CPA, Data Science International). After 2 h of stable basal telemetry measurements, an injection of VEGF (25 ng, i.c.v.) or vehicle (PBS 1μl, i.c.v.) was randomly given and BP and HR responses were recorded for the next 5 h.

Central effects of VEGF on blood pressure, heart rate and renal sympathetic nerve activity in anesthetized mice

On the day of the study, each mouse was anesthetized with intraperitoneal administration of Ketamine (91 mg/kg, BW) and Xylazine (9.1 mg/kg, BW) then underwent intubation with PE-50 to provide an unimpeded airway for the mouse to spontaneously breathe O_2-enriched room air. A micro-renathane tubing (MRE-40, Braintree Scientific) was inserted into the right jugular vein for intravenous infusion of the anesthetic agent: α-chloralose (initial dose: 12 mg/kg, then a sustaining dose of 6 mg/kg/h). Another MRE-40 catheter was inserted into the left carotid artery and connected to a pressure transducer (BP-100; ADInstruments) for continuous measurement of BP and HR. Core body temperature, monitored through a rectal probe, was maintained at 37.5°C with a temperature controller. A left retroperitoneal incision was made to access the postganglionic nerve fibers that subserve the left kidney (rSNA). After careful isolated from surrounding connective tissues, a bipolar platinum-iridium electrode (36-gauge, A-M Systems) was suspended under the renal nerve fascicle and secured with silicone gel (Kwik-Sil, WPI). The electrode was attached to a high-impedance probe (HIP-511, Grass Instruments) and the nerve signal was amplified 10^5 times and filtered at a 100- and 1000-Hz cut-off with a Grass P5 AC pre-amplifier. The amplified and filtered nerve signal was routed to a speaker system and to an oscilloscope (model 54501A, Hewlett-Packard) to monitor the audio and visual quality of the sympathetic nerve recordings. For quantification purposes; the amplified, filtered nerve signal was directed to a resetting voltage integrator (model B600c, University of Iowa Bioengineering, IA, USA) and to a MacLab analogue-digital converter (Model 8S, ADInstruments Castle Hill, New South Wales, Australia) containing the software (MacLab Chart Pro; Version 7.0) that utilizes a cursor to analyze the number of spikes/second that exceeds the background noise threshold. Baseline BP, HR and rSNA were recorded over a 10 min control period before i.c.v. injection of VEGF (25 ng) or Vehicle (PBS: 1 μl) was made. The rSNA response was continuously recorded and quantified at 15 min intervals over the next 4 h. Any residual

nerve activity that remained after death was considered background noise and thus was subtracted from the measured SNA for both resetting voltage integration and spikes/s. The experiment was conducted in a non-blinded fashion.

Leptin administration *in vivo*

Repeated intraperitoneal leptin administration protocol

5 mg of recombinant mouse leptin (498-OB, R&D systems, Minneapolis, US) was dissolved in 1 ml ice-cold Tris-HCl buffer (20 mM, pH 8). This stock solution (5 mg/ml) was further diluted with ice-cold PBS (pH 7.4) to get a 1 mg/mL working solution. For vehicle control injections, the equivalent volume of plain 20 mM Tris-HCl was diluted in ice-cold PBS (pH 7.4). Whenever indicated, mice received repetitive leptin administration 3 mg/kg BW i.p. twice daily over two days plus another terminal injection in the following morning. Mice were sacrificed by transcardial perfusion 45 min following the injection to allow for immunohistochemical detection of pSTAT3 or 30 min post-injection for $pERK_{1/2}$. In acute studies, mice received 5 mg/kg BW leptin i.p. 90 min before sacrifice to determine HIF1α induction by means of Western blot and HIF1A-1/ODD luciferase activity.

Intracerebroventricular delivery of leptin to $Lep^{ob/ob}$ mice

The pro-angiogenic effect of leptin was studied in homozygous $Lep^{ob/ob}$ mice and heterozygous $Lep^{ob/+}$ littermates at 12 weeks of age. Intracerebroventricular (i.c.v.) cannula and micropump implantations were performed as previously described (Ducy et al., 2000; Sato et al., 2007). In brief, a cannula was implanted into the cerebral lateral ventricle (AP: −0.50 mm, ML: ± 1.3 mm, DV: −2.3 mm), and an osmotic micropumps (model 1002D, Alzet) was implanted subcutaneously *via* a catheter connected to the cannula. Micropumps were loaded with either high-dose leptin (200 ng/day), low-dose leptin (50 ng/day) or vehicle (aCSF) the day prior to surgery. Food intake and bodyweight loss was controlled daily. High-dose leptin group was terminated prior (day 7 post-surgery) due to the culminating anorexia whereas all remaining groups were terminated at day 10 post-surgery.

Analysis of serum leptin concentrations in mice

Food was removed from mice for 3 h in the morning. Blood was collected from the tail vein into microvette tubes and immediately stored on ice in order to obtain serum (5,000 x g for 10 min at 4°C). Serum leptin concentrations determined by a commercial mouse leptin ELISA (Alpco) following the manufacturer's instructions.

Glucose metabolism in mice *in vivo*

Before glucose tolerance tests, mice were fasted for 4 h and then given an intraperitoneal injection of glucose dissolved in 1xPBS (pH 7.4) at 2 g/kg BW. Glycemia was measured by sampling blood from the tail vein before (0 min) and at 15, 30, 60 and 120 min post injection *via* a handheld glucometer (Abbott, Wiesbaden, Germany). In order to assess insulin sensitivity, additional blood was collected at 0 min using EDTA-coated microvette tubes (Sarstedt, Nürnbrecht, Germany) to obtain plasma (5,000 x g for 10 min at 4°C). Insulin concentration was determined using a commercial insulin ELISA following the manufacturer's instructions (Ultra-sensitive Mouse Insulin ELISA Kit, #90080 Crystalchem, Netherlands). HOMA-IR was calculated using the formula: HOMA-IR=[fasting insulin (mU/l) * fasting glucose (mg/dl) / 405] (Matthews et al., 1985).

Viral targeting of astrocytic VEGF signaling in the mediobasal hypothalamus (MBH)

In order to manipulate *Vegfa* expression levels in the MBH, recombinant adeno-associated viruses of serotype 2/5 ($AAV_{2/5}$) were commercially generated (VectorBioLabs, Malvern, US) and configured such that viral transgene expression was driven in each case from a synthetic 2.2 kb GFAP promoter element (Gfa2) faithfully restrictive to astrocytes as described previously (Brenner et al., 1994). Respective AAVs were injected bilaterally (0.5 µl per hemisphere; 1.0×10^{12} viral genomes/ml) using a stereotaxic system combined with a binocular 3.5x-90x stereomicroscope (AMScope, USA) and a 2 µl syringe (2 µl with a 30 G needle; Hamilton, US). Injection speed was set at 250 nl/min and undesired diffusion of viral particles was further prevented by slow retraction of the cannula 5 min post injection. The following stereotaxic coordinates were obtained from 'The Mouse Brain in Stereotaxic Coordinates' (Franklin and Paxinos, 2008) and used to target the MBH of the mouse brain: −1.4 mm posterior and ±0.2 mm lateral to the bregma and −5.8 mm ventral from the dura mater. Anesthesia was performed by a mixture of ketamine and xylazine (100 mg/kg BW and 7 mg/kg BW, respectively) while acute Metamizol (200 mg/kg, subcutaneous) followed by Meloxicam (1 mg/kg, on three consecutive days, subcutaneous) was administered for postoperative analgesia.

Knockdown of *Vegfa* mRNA in astrocytes was achieved by using an AAV2/5 variant (AAV.shRNA(VEGF) $^{v\Delta GFAP/+}$) driving GFP expression together with a shRNA targeted against *Vegfa* separated by a P2A linker peptide within the GFP 3'UTR. The following targeting sequence was selected after providing >60% knockdown efficiency in an initial validation screen: *TGAAGATGTACTC-TATCTCGT (nt1218-1238 of NM_009505)*. This sequence was further fused to the following hairpin loop sequence: GTTTTGGCCACTGACTGAC. Control AAV was identical except for carrying a scrambled RNA sequence (AAV.scrmbl.RNA$^{GFAP/+}$). Respective AAV's were injected into male C57BL/6J mice that were either fed a HFHS diet 10 d post injection or that already had established diet-induced obesity.

Restoration of *Vegfa* expression in hypothalamic astrocytes devoid of HIF1α was achieved by using a combination of the following AAV2/5 variants to be injected into the MBH of HIF1α $^{loxP/loxP}$ mice: (1) AAV.Gfa2.iCre $^{+}$ expressing codon-optimized Cre recombinase (Cat. No: VB1172) combined with (2) AAV.Gfa2.$VEGF_{GFP}$ driving the expression of *Vegfa164* together with GFP separated by a by a P2A linker peptide (AAV2/5.Gfa2-GFP-2A-m-VEGF-a; Cat.No: AAV-275992; RefSeq#:BC061468; VectorBioLabs, Malvern, US). As control groups, mice were either injected with AAV.Gfa2.iCre (VB1172; VectorBioLabs, Malvern, US) (HIF1α knockout group) or injected with AAV.Gfa2.EGFP (VB1180; VectorBioLabs, Malvern, US) (control). Mice were switched to HFHS diet 10 d post injection.

In vivo bioluminescence imaging of HIF1A/ODD-Luciferase mice

Food was removed from homozygous HIF1A/ODD-Luc mice 3 h prior to the experiment. Pairs of mice received either vehicle or leptin (5 mg/kg BW; i.p.) followed by another injection 50 min thereafter with the improved luciferin analog CycLuc1 (100 μl of 10 μM; i.p.). 60 minutes after the injection, pairs of anesthetized mice were placed in an IVIS Spectrum *in vivo* imaging system (PerkinElmer). Luminescent exposure was set at 60 s with an open emission filter and binning factor 8. For image acquisition, a field of view 6.6 cm was used along with subject size of 1.5 cm (mouse).

Ex vivo luciferase assay of HIF1A/ODD-Luc brain homogenates

Luciferase activity in mouse hypothalamus and cortex was assessed as previously described (Hoppe et al., 2016). Briefly, HIF1A/ODD-Luc mice were sacrificed upon food removal for 3 h, their hypothalami and cortex were rapidly dissected and homogenized in Glo Lysis Buffer (Promega) using a glass homogenizer (Duran Wheaten Kimble, US) on ice. Cell debris was spun down at 10,000 x g, 4°C for 10 min. Protein concentration of supernatant was determined using BCA protein assay (ThermoFisher Scientific, Rockford, IL US) and adjusted to 250 μg in a final volume of 100 μl of Glo Lysis Buffer (Promega). Samples were placed in a white opaque 96-well plate, brought to room temperature and mixed with an equal volume (100 μL) of ready-to-use luciferase substrate Bright-Glo Luciferase Assay System (Promega), and luminescence was measured immediately by a luminometer (PheraStar F; BMG LABTECH GmbH, Ortenberg, Germany).

Vascular reactivity experiments in aorta segments

For the vascular reactivity experiments, the aorta was carefully dissected, cut in 2 mm segments and kept in cold isotonic saline. Each aorta segment was set in a 4 ml organ bath containing modified Krebs–Henseleit solution (mM) (NaCl, 115; KCl, 4.6; KH_2PO_4, 1.2; $MgSO_4$, 1.2; $CaCl_2$, 2.5; $NaHCO_3$, 25; glucose, 11) at 37 °C. The solution was equilibrated with 95% oxygen and 5% carbon dioxide to a pH of 7.3–7.4. For the setting process, two fine steel wires (100 μm diameter) were passed through the lumen of the vascular segment. One wire was attached to the organ bath wall and the other wire was connected to a strain gauge for isometric tension recording (Universal Transducing Cell UC3 and Statham Microscale Accessory UL5, Statham Instruments). This arrangement permits applying passive tension in a perpendicular plane to the long axis of the vascular cylinder. The changes in isometric force were recorded using a PowerLab data acquisition system (ADInstruments, Colorado Springs, CO, US). After applying an optimal passive tension of 1 g, vascular segments were allowed to equilibrate for 60–90 min. Afterwards, segments were stimulated with potassium chloride (KCl 100 mM) to determine the contractility of smooth muscle. Segments which failed to contract at least 50 mg to KCl were discarded. After equilibration, the segments were pre-contracted with the analogue of thromboxane A2 U46619 (10^{-8} M) (Sigma-Aldrich, St. Louis, MO, USA). Then, in order to assess the endothelium-dependent and endothelium-independent relaxation, cumulative dose-response curves in response to acetylcholine (ACh) (10^{-9}-10^{-4} M) and sodium nitroprusside (10^{-9}-10^{-4} M) (Sigma-Aldrich) were performed. The relaxation in response to ACh was determined based on the percentage of the active tone achieved by the NO donor sodium nitroprusside (10^{-5} M) (Sigma-Aldrich). For each dose–response curve, the maximum effect (E_{max}) and the logarithm of the concentration producing 50% of the maximal response (ED_{50}) was calculated by geometric interpolation.

Magnetic-activated and fluorescence-assisted cell sorting (MACS/FACS)

In order to validate the efficient deletion of exon 2 in HIF1α flox/flox mice, we generated dual fluorescent reporter mice (HIF1α $^{loxP/loxP}$::hGFAP.CreER^{T2}::ROSA26$^{mT/mG}$) allowing us to differentiate non-recombined (tdTomato$^+$EGFP$^-$) from recombined (tdTomato$^+$EGFP$^+$) astrocytes for separate downstream analyses. Cre-mediated recombination was induced by tamoxifen injection at the age of 6 weeks as described before (10 mg/5 d). At 12 weeks of age, mice were sacrificed, their brains were rapidly removed and one hemisphere per mouse was subjected to magnetic-bead assisted cell sorting (MACS) enrichment using the astrocyte-specific surface marker ACSA-2 (Batiuk et al., 2017; Kantzer et al., 2017). ACSA-2$^+$ astrocytes were enriched according to a commercially available standard protocol (Isolation and Cultivation of Astrocytes from Adult Mouse Brain; Miltenyi Biotec) using LS columns and an elution volume of 1 mL PBS. Cells were then rapidly subjected to fluorescence-activated cell sorting (FACS) in order to further separate recombined from non-recombined ACSA-2+ tdTomato+ astrocytes based on EGFP expression. To accurately gate the aforementioned subpopulations, a non-tamoxifen injected littermate reporter mouse (tdTomato$^+$ EGFP$^-$ ACSA-2$^+$) and a non-fluorescent C57BL/6J wildtype mouse (tdTomato$^-$ EGFP$^-$ ACSA-2$^+$) were initially analyzed by FACS. Sorting was performed using a FACSAria III (BD Biosciences, Heidelberg, Germany) with an 85 μm nozzle. For optimal visualization of all ACSA-2+ astrocytes, logarithmic scales and low acquisition voltages (75 and 190) were implemented for forward scatter (FSC) and side scatter (SSC) plots, respectively. Sorted cells were collected in cold PBS, pelleted by centrifugation for 5 min at 600 x g and 4°C, resuspended in 350 μl RLT buffer supplemented with 0.4 mM DTT and stored at -80°C until RNA extraction (RNeasy MicroKit; Quiagen) and cDNA synthesis (SMARTer PCR cDNA synthesis kit; TaKaRa) following manufacturer's indications.

In a separate set of mice, the reduction in astrocytic *Hif1α* expression was compared between hGFAP.CreER^{T2}::ROSA26$^{mT/mG}$ mice that harbour either wildtype alleles for HIF1α (HIF1α $^{wt/wt}$) or both alleles with exon 2 flanked by loxP sites (HIF1α $^{loxP/loxP}$). Cre-mediated recombination was induced by tamoxifen injection at the age of 6 weeks as described before (10 mg/5 d). At 12 weeks of age, mice were sacrificed, their brains were rapidly removed, the hypothalami were collected and recombined astrocytes (tdTomato$^+$EGFP$^+$) were magnetically separated via MACS by using a GFP-antibody coupled to magnetic beads (μMACS GFP isolation kit, Miltenyi Biotec). As for pre-enrichment for ACSA-2$^+$ astrocytes, the commercially available standard protocol was followed (Isolation and Cultivation of Astrocytes from Adult Mouse Brain; Miltenyi Biotec) using LS columns and an elution volume of 1 mL

PBS. For quantitatively assessing HIF1a expression *via* qPCR, a TaqMan probe was selected that span exon 2 that is flanked by loxP sites.

Fluorescent angiography

To obtain detailed information of the mouse brain vascular profile, animals were sacrificed with CO_2 and transcardially perfused with 20 ml phosphate-buffered saline (PBS) (GibcoTM, pH 7.4) supplemented with Lectin-FITC conjugate (25 μg/ml; *Tritium vulgaris*; L4895; Merck, Germany) by using a peristaltic pump at 120 mmHG (Instech, High Flow P720 equipped with 21G canula). Cohorts of animals already expressing green-fluorescent reporter proteins were perfused with an alternative vessel dye (wheat heat-germ agglutinin (WGA) conjugated to fluorchromophores Alexa Fluor 647; W21404; ThermoFisher, Germany). Perfusions were finalized with 20 ml of 4% paraformaldehyde (PFA) in PBS, pH 7.4, brains were removed and post-fixed in 4% PFA at 4°C. In order to rule out potential confounding by applying a uniform pressure source in perfusion-based angiography, we subjected one cohort of mice to intravenous administration of FITC-albumin (10 mg/ml in 0.9% NaCl; MW 69 kDa, Merck, Germany), which was infused slowly into the tail vein over 5 min. After 8 more min in which the dye was allowed to become distributed solely by means of cardiovascular function, mice were decapitated and brains rapidly immersion-fixed in 4% PFA in 0.1 M PBS (pH 7.4) for 72 h at 4°C. In either case, brains were then equilibrated with 30% sucrose in Tris-buffered saline (TBS, pH 7.2) for 48 h before being sectioned into 40 μm coronal slices using a cryostat (CM3050S; Leica, Germany). Three to four brain sections per mouse were selected containing the middle portion of the MBH and either directly mounted on gelatine-coated glass slides, dried and cover-slipped by a polyvinyl alcohol (mowiol, Merck, Germany) mounting medium supplemented with DABCO (Merck, Germany) or further subjected to additional immunohistochemistry.

Assessment of blood-brain barrier integrity

Properties of the blood-brain barrier were analyzed by immunohistochemical detection of endogenous albumin (ca. 68 kDa) extravasating into the parenchyma (indicative of protein permeability). In another set of animals, we administered the exogenous tracer FITC-Dextran 40 kDa (100 ul of 100 mg/ml; i.v.). In order to avoid diffusion and washout of low-molecular tracers we employed a specific histological preparation technique described previously (Hoffmann et al., 2011). In brief, tracer was allowed to circulate for 5 min, mice were sacrificed by rapid decapitation and brains were immersion fixed for 48h at 4°C. Brains were frozen upon brief (> 12 h) dehydration in 30% sucrose and cut at a cryostat at 50 μm. Coronal brain sections were immediately mounted and cover-slipped without rehydration.

Image acquisition and analysis of vascularity in consecutive brain sections

Images were acquired as z-stacks using a confocal microscope (Leica TCS SP5 and SP8, Germany) with an air-immersed 20x objective (mice) or 10x objective (rats) with 2 μm step size in the z-direction. ImageJ/FIJI was used to trace and manually quantify the length of fluorescently labelled vessels in the MBH. The mean length of vasculature within the MBH (hemisection) was calculated for each experimental group. For high-magnification assessment of e.g. vascular basement membranes, vascular permeability towards albumin or FITC-Dextran (40 kDa) co-localization analysis, a glycerol-immersed 63x objective was used.

Brain sectioning and immunohistochemistry

Brains were post-fixed overnight in 4% PFA at 4°C, followed by equilibration with 30% sucrose in Tris-buffered saline (TBS, pH 7.2) for 48 h before being sectioned into 40 μm coronal slices using a cryostat (CM3050S; Leica, Germany). Three to four brain sections per mouse were selected containing the middle portion of the MBH and subjected to the immunohistochemical protocol. Brains were first washed with TBS and incubated overnight at 4°C with primary antibodies (anti-VEGF 1:500; anti-GFAP 1:1000; anti-claudin-5 1:300; anti-albumin 1:500; anti-Iba1 1:1000; anti-Ki67 1:500; anti-NeuN 1:300; anti-pSTAT3 ^{TYR} 1:500; anti-p$ERK_{1/2}$ 1:500) in a solution containing 0.25% porcine gelatine and 0.5% Triton X-100 in TBS, pH 7.2. The next morning, sections were serially rinsed in TBS, pH 7.2, and incubated with respective secondary antibodies all diluted 1:1000 in TBS, pH 7.2 containing 0.25% porcine gelatine and 0.5% Triton X-100 for 2h. Sections were serially washed in TBS with the last washing additionally containing DAPI (2 μg/ml in TBS, pH 7.2) in order to facilitate the demarcation of brain region for downstream image analyses. Where indicated, sections were additionally treated with fluorescent Nissl stain (1:100 NeuroTraceTM 435/455 or 500/525; ThermoFisher, Germany) to identify neuronal cells.

Immunostaining for pSTAT3 and p$ERK_{1/2}$

Slight adjustments of this basic protocol were implemented for the immunohistochemical visualization of pSTAT3 ^{TYR} (1:500) and p$ERK_{1/2}$ (p-42/44 MAPK; 1:500) such that brain sections were pre-incubated in 100% methanol at -20°C for 15 min.

Immunostaining for laminin and collagen-IV

In the adult, formalin-fixed mouse brain, most basement membrane proteins tend to be inaccessible for immunohistochemical labelling. We hence applied a specific antigen retrieval protocol to unmask vasculature-associated laminin (1:300) and collagen IV (1:300) as described previously (Franciosi et al., 2007). In brief, pepsin digestion was carried out on free-floating sections with pre-incubation in distilled water for 5 min at 37°C before being transferred to 1 mg/ml pepsin (Dako, Carpinteria, CA) in 0.2 N HCl for 10 min at 37°C.

3DISCO-assisted optical clearing of whole brains

To obtain three-dimensional information of the global mouse brain vasculature, animals were transcardially perfused with a vessel tracer conjugated to a fluorochromophor with emission peaks in the far-red range (WGA-Alexa Fluor 633; ThermoFisher, Germany) in order to overcome tissue autofluorescence, to facilitate light penetration and to improve the signal-to-background ratio. Following the perfusion with 4% PFA and the overnight post-fixation in 4% PFA, brains were washed three times in PBS, pH 7.4, before being subjected to an organic solvent-based, optical clearing protocol (3DISCO) described previously (Ertürk et al., 2012). In brief, brains were serially incubated in 50%, 70%, 80% and 100% (v/v) of tetrahydrofuran (THF) at room temperature on a shaker for 1 h followed by incubation in 100% v/v THF overnight. The next morning, THF was refreshed and brains were incubated for another hour. De-lipidation of brains was achieved by incubation in dichloromethane (DCM) for 1 hour at room temperature. Finally, brains were optically cleared by immersion in BABB (benzyl alcohol:benzyl benzoate; 1:2) and stored within until image acquisition.

Light-sheet microscopy imaging

Mouse brains were placed into the imaging chamber having its reservoir filled with the final clearing solution (BABB) in order to match the refractive indices. Importantly, brains were oriented upright and single-plane illuminated (light-sheet) image stacks were acquired along the rostrocaudal axis for maximal coronal resolution. Image acquisition was carried out at an Ultramicroscope II (LaVision BioTec), featuring an axial resolution of 4 μm with the following filter sets: ex 640/40 nm, em 690/50 nm. For high magnification-whole-brain imaging of the global mouse brain vasculature, a 4x Olympus objective was used (Olympus XLFLUOR 4x corrected/0.28 NA [WD = 10 mm]) combined with an Olympus revolving zoom body unit (U-TVCAC). Keeping the zoom factor as 1x and setting 2x3 tile scans with 20% overlap, we imaged a field of view of 6.14 x 8.82 mm, covering the entire width and depth of the mouse brain from the rostral surface to the cerebellum region up to 7.2 mm using a z-step of 8 μm. Exposure time was 70 ms, laser power was adjusted depending on the intensity of the fluorescent signal (in order to never reach the saturation) and the light-sheet width was kept at maximum. For high resolution imaging of the hypothalamus area, a 2x Olympus objective (Olympus MVPLAPO2XC/0.5 NA [WD = 6 mm]) attached to an Olympus MVX10 zoom body was used with a zoom factor at 1.25. Single z-stack scans were taken from the ventral surface of the brain to 3.5-4.5 mm in depth using a z-step of 6 μm to cover the entire hypothalamus.

Analysis of vascularity in 3D whole-brain data sets

Whole-brain coronal stacks were loaded in ImageJ/FIJI and divided into sub-stacks in which pre-defined masks were used to crop out selected brain regions from each hemisphere (LS: lateral septum, CPu: caudate putamen, NAcc: nucleus accumbens, S1BF: somatosensory cortex barrel field, HIPP: hippocampus, PVN: paraventricular nucleus, DMH: dorsomedial hypothalamus, LH: lateral hypothalamus, VMH: ventromedial hypothalamus, ARC: arcuate nucleus). Given slight differences in clearing efficiency across brain regions, individual thresholds were applied for each sub-stack. Next, sub-stacks were subjected to a filter function of 2 pixel at median intensity before being binarized and skeletonized. Each coronal single plane was analyzed by using the histogram function of ImageJ/FIJI in order to relatively quantify vascular versus non-vascular pixels. Means of all individual planes derived from a respective brain region were calculated per hemisphere.

Analysis of MBH vascularity of consecutive confocal micrographs

Image files (z-stacks at 2 μm step size) were imported to FIJI/ImageJ and converted into maximum projections. A pre-defined region-of-interest was cropped out, binarized and subjected to individual thresholding. Total vessel length of hemisection MBH was assessed by manual tracing of the vascular network.

Analysis of basement membrane thickness

Scans of brain sections immunostained for both collagen-IV and laminin were imported to FIJI/ImageJ and converted into maximum projections. Transversely cut blood vessels were selected and the thickness of both collagen-IV and laminin immunoreactivity was assessed by averaging the width of immunoreactivity perpendicular to three randomly chosen tangents.

Electron microscopy

Mice were anaesthetized and perfused transcardially with 0.9% saline followed by fixative containing 4% paraformaldehyde and 0.1% glutaraldehyde. After overnight (4°C) post-fixation in glutaraldehyde-free fixative, 50-micron vibratome sections (Pelco Easy-Slicer; Ted Pella, Redding, CA, USA) were cut. The sections were osmicated in 1% osmium tetroxide, and dehydrated in increasing ethanol concentrations. 1% uranyl acetate was added to the 70% ethanol to enhance ultrastructural membrane contrast. Flat embedding in Durcupan followed dehydration. Ultrathin sections were cut on a Leica ultramicrotome (Leica Microsystems, Buffalo Grove, IL, USA). The sections were collected on Formvar coated slot grids, and analyzed with a Tecnai 12 Biotwin electron microscope (ThermoFisher Scientific, Hillsboro, OR, USA). Endothelial basal membrane thickness was assessed at 4900 magnification.

Protein extraction and Western blotting

Protein content of hypothalamic tissue was extracted using RIPA buffer supplemented with 200 μM CoCl2 (Sigma-Aldrich Chemie GmbH, Taufkirchen, Germany) and protease and phosphatase inhibitors (1% v/v; ThermoFisher Scientific, Rockford, IL US) in a final volume of 80 μl using a glass homogenizer (Duran Wheaten Kimble, US). Cellular debris was centrifuged at 10,000 x g at 4°C for 10 min and protein concentration of the supernatant was determined using BCA protein assay (ThermoFisher Scientific, Rockford,

IL US). Protein was adjusted to 30 μg per sample, complemented with Laemmli loading buffer plus 10% β-mercaptoethanol, denatured by heating at 95°C for 10 min and separated by molecular weight using SDS-PAGE. Protein was blotted on 0.45 μm PVDF membranes and blocked in 5% skimmed milk in TBS with 0.1% Tween-20 (TBS-T) for one hour at room temperature. Membranes were incubated with primary antibodies (anti-HIF1α 1:1000) overnight at 4°C, serially washed in TBS-T and incubated with the respective HRP-coupled secondary antibodies (anti-β-actin 1:5000) for one hour at room temperature. Membrane development was carried out with chemiluminescent HRP substrate (Immobilion Western, Millipore) using films (Hyperfilm ECL, GE Life Sciences; CL-XPosure Film, ThermoFisher Scientific).

RNA isolation and qPCR analysis

RNA was isolated from tissues or primary mouse astrocytes using a commercially available kit (MircoRNeasy Kit, Qiagen, Hilden, Germany). Identical amounts of RNA were reverse-transcribed to cDNA using Superscript III (Invitrogen, Darmstadt, Germany) and gene expression was analyzed using TaqMan probes (ThermoFisher Scientific, Rockford, IL USA) at a ViiATM7 Real Time PCR System or QuantStudio 6 FLEX Real Time PCR System (ThermoFisher Scientific, Rockford, IL USA). Expression changes were calculated using the $2^{-\Delta\Delta Ct}$ method normalized by Hprt or Rpl32 as housekeeping genes. In order to determine the presence of LepR isoforms in cDNA derived from magnetic-assisted cell sorted astrocytes the following primers were used as previously described (Hsuchou et al., 2009): $LepR_a$ (forward primer: GAAGTCTCTCATGACCACTACAGATGA; reverse primer: TTGTTTCCCTCCATCAAAATGTAA; product size 98 bp). $LepR_b$ (forward primer: GCATGCAGAATCAGTGATATTTGG; reverse primer: CAAGCTGTATCGACACTGATTTCTTC; product size 81 bp).

QUANTIFICATION AND STATISTICAL ANALYSIS

Data analysis was conducted using GraphPad Prism (Version 6). No power calculations were used to predetermine sample sizes. Sets of data were analyzed by linear regression analysis, Student's t-test, or one- or two-way analysis of variance (ANOVA) with Tukey post-hoc analyses to determine statically significant differences. Normal distribution of populations at the 0.05 level was tested using the D'Agostino-Pearson omnibus normality test. Data were screened using the maximum normal residual Grubb's test to identify singular, statistically significant outliers. Exclusion criteria of samples included mistargeting of AAV injections (2 mice in $HIF1\alpha^{AAV.Gfa2.iCre}$ and $HIF1\alpha^{AAV.Gfa2.iCre + VEGF}$, respectively) and poor perfusion-based vascular labelling (5 mice in TRE-Lep^{rtTA} and 3 mice in $HIF1\alpha^{i\Delta astro/GLAST+}$ mice). p values ≤ 0.05 were considered statistically significant. Cohorts of mice receiving AAV nanoinjections were randomly assigned to respective groups; thus, bodyweight-matched littermates received either of the respective AAVs while remaining group housed for the duration of the experiment. Inducible knockout models were bred following a heterozygous x wildtype scheme ($CreER^{T2}$ allele); offspring were born at expected mendelian ratios, what determined group composition since all littermates were treated with tamoxifen as previously indicated. All data are presented as mean ± standard error (SEM) and all p values as well as n are reported in the individual figure legends.